

# SEAFLOOR SPREADING AND TECTONICS AT THE CHARLIE GIBBS TRANSFORM SYSTEM (52-53°N, MID ATLANTIC RIDGE): PRELIMINARY RESULTS FROM *R/V A. N. STRAKHOV* EXPEDITION S50

Sergey G. Skolotnev\*, Alessio Sanfilippo\*\*<sup>✉</sup>, Alexander A. Peyve\*, Yago Nestola\*\*\*, Sergey Yu. Sokolov\*, Lorenzo Petracchini\*, Kseniya O. Dobrolyubova\*, Valentin Basch\*\*, Alexey N. Pertsev°, Carlotta Ferrando\*\*, Alexander N. Ivanenko°, Camilla Sani\*\*, Anatoly A. Razumovskiy\*, Filippo Muccini<sup>°°°</sup>, Artem S. Bich§, Camilla Palmiotta\*\*\*, Yuri V. Brusilovsky°, Enrico Bonatti\*\*\*§§, Konstantin N. Sholukhov°, Marco Cuffaro°, Ilya A. Veklich°, Vitaly N. Dobrolyubov\* and Marco Ligi\*\*\*

\* *Geological Institute, Russian Academy of Sciences, Moscow, Russia.*

\*\* *Dipartimento di Scienze della Terra e dell'Ambiente, Università di Pavia, Italy.*

\*\*\* *Consiglio Nazionale delle Ricerche, ISMAR, Bologna Italy.*

• *Consiglio Nazionale delle Ricerche, IGAG, Roma, Italy.*

° *Institute of Geology of Ore Deposits, Petrography, Mineralogy and Geochemistry, Russian Academy of Sciences, Moscow, Russia.*

°° *Shirshov Institute of Oceanology, Russian Academy of Sciences, Moscow, Russia.*

°°° *Istituto Nazionale di Geofisica e Vulcanologia, Via di Vigna Murata, Roma, Italy.*

§ *FSBI «VNIIOkeangeologia», Saint-Petersburg, Russia.*

§§ *Lamont Doherty Earth Observatory of Columbia University, Palisades, New York, USA.*

✉ *Corresponding author, e-mail: alessio.sanfilippo@unipv.it*

**Keywords:** *Mega-transform, Charlie Gibbs Fracture Zone, Oceanic Core Complex.*

## ABSTRACT

The Charlie Gibbs offsetting by ~ 340 km the Mid Atlantic Ridge (MAR) axis at 52°-53° N is one of the main transform systems of the North Atlantic. Located between long mid-ocean ridge segments influenced from the south by the Azores and from the north by the Iceland mantle plumes, this transform system has been active since the early phases of North Atlantic rifting. Object of several surveys in the '70 and '80, Charlie Gibbs received great attention for its unique structure characterized by two long-lived right-lateral transform faults linked by a short ~ 40 km-long intra-transform spreading centre (ITR) with parallel fracture zone valleys extending continuously towards the continental margins. In October 2020 expedition S50 of the *R/V A.N. Strakhov* surveyed an area of 54,552 km<sup>2</sup> covering the entire Charlie Gibbs transform system and the adjacent MAR spreading segments. We collected new bathymetric, magnetic and high-resolution single channel seismic data, along with basaltic, gabbroic and mantle rocks from 21 dredges. This work contains preliminary data from cruise S50 and discusses the large-scale architecture of this unique, long-lived transform system.

## INTRODUCTION

The mantle plumes centred on Iceland and Azores strongly affect the composition and the thermal state of the mantle beneath the MAR in the North Atlantic. These two major plumes affect the bathymetry and the geochemistry of the basalts, tracers of the mantle composition. These two large-scale upper mantle plumes are separated by the Charlie Gibbs Fracture Zone (FZ) located at a latitude of ~ 52° 30' N (Fig. 1), arguably one of the most prominent tectonic features of the North Atlantic (e.g., Searle, 1981; Whitmarsh and Calvert, 1986). Two transform faults linked by a short ~ 40 km-long intra-transform spreading centre, offset left-laterally the MAR axis by about 340 km (e.g., Johnson, 1967; Fleming et al., 1970; Searle, 1981; Calvert and Whitmarsh, 1986; Whitmarsh and Calvert, 1986). The trace of these transforms can be followed for thousands of kilometres towards the continental margins (e.g., Olivet et al., 1970; 1974) suggesting they have been active since the initial stages of continental breakup between North America and Europe (e.g., Roberts et al., 1979), and during the evolution of the North Atlantic since Cretaceous time (e.g., Srivastava et al., 1988a; 1988b; Srivastava and Verhoef, 1992). The progressive changes

in the direction of extension during rifting and of seafloor spreading after the onset of oceanization resulted in structural complexity of the continental margins and of the oceanic lithosphere of this portion of the Atlantic (e.g., Keen et al., 2014; Peace et al., 2019). The preservation of two parallel fracture zones indicates that the short intra-transform spreading segment that links the two Charlie Gibbs transforms stayed active since the early stages of opening of the North Atlantic. This contrasts with the morphological complexity documented in some long-offset transforms of the Equatorial Atlantic, such as Romanche (e.g., Bonatti et al., 1994; Ligi et al., 2002; 2005), St. Paul (e.g., Melson et al., 1973; Bonatti et al., 1992; Maia et al., 2016) and Doldrums (e.g., Bonatti et al., 1992; Skolotnev et al., 2020). There, changes in plate kinematics have led to the activation or deactivation of intra-transform spreading centres forming lens-shaped structures, reaching locally hundreds of kilometres in width including several active transform segments (e.g., Ligi et al., 2002; Skolotnev et al., 2020). Although the formation of these intra-transform domains appears to be driven mainly by changes in plate motion and is ultimately related to far-field forces (Bonatti, 1978; Maia et al., 2016), the composition of the mantle may play a major role in determining the style and

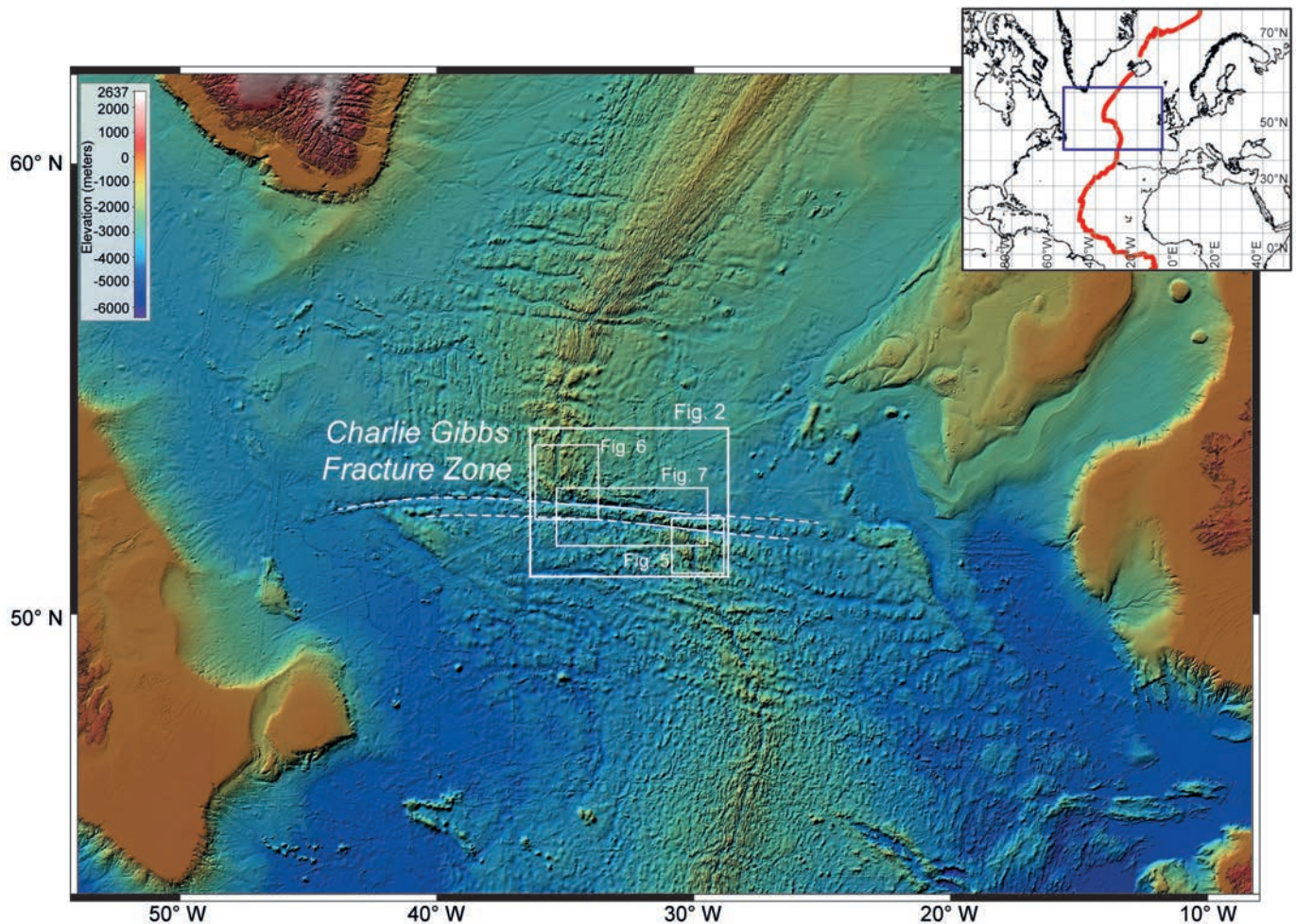


Fig. 1 - Compilation of bathymetric data (GEBCO) of the northern Mid-Atlantic Ridge and location of the Charlie Gibbs transform. White dashed lines indicate the two fracture zone troughs and white boxes indicate locations of Figs. 2, 5, 6 and 7.

location of magmatism along large-offset transform domains (e.g., Chernysheva and Kharin, 2009). In turn, this has an important impact on the rheology of the lithosphere and style of seafloor spreading.

The Charlie Gibbs region was investigated mostly by geophysical surveys during the seventies (Fleming et al., 1970; Vogt and Avery, 1974; Lonsdale and Shor, 1979; Searle, 1981). The large-scale structure was initially described by Johnson (1967) and mapped in more detail during later expeditions (Fleming et al., 1970; Olivet et al., 1974; Lonsdale and Shor, 1979; Searle, 1981; Smoot and Sharman, 1985; Whitmarsh and Calvert, 1986). Sampling of the Charlie Gibbs FZ has been conducted in the late '60s with the *R/V Jean Charcot* (1969; Hekinian and Aumento, 1973) and '70s with the *C.S.S Dawson* (1970; e.g., Hekinian and Aumento, 1973; Sigurdsson, 1981; Shilling et al., 1983) and *R/V Akademik Kurchatov* (1973; Shilling et al., 1983; Chernysheva and Kharin, 2009).

After more than 40 years, some Irish expeditions (CE15007-Marine Institute of Ireland, CE16014-Geological Survey of Ireland and CE18008-University College of Dublin with *R/V Celtic Explorer*) recently surveyed a portion of the intra-transform region showing linear hills oriented sub-parallel to the spreading direction defining “corrugated surfaces” on the tops of domed massifs. These structures, called “megamullions” or oceanic core complexes (OCCs), indicate that large sections of lower oceanic crust and abyssal mantle

are potentially exposed within the two fracture zones, east and west of the Charlie Gibbs intra-transform spreading centre (ITR).

In this study, we present new data collected during cruise S50 with the *R/V Akademik Nikolaj Strakhov* (September-October 2020). We provide here a first complete bathymetric image of the Charlie Gibbs transform system including the adjacent southern and northern MAR segments (Fig. 2). High resolution multibeam data, single channel seismic and magnetic profiles were acquired. Dredges were deployed along the ridge axes, at transform walls and along corrugated surfaces of bathymetric highs. This sampling is of particular interest considering the paucity of basaltic samples reported to date in the studied area. The new morphological images, seismic and magnetic data, and dredge results are reported here to discuss preliminary hypotheses on the large-scale structure of this major transform domain.

## CHARLIE GIBBS TRANSFORM SYSTEM

The Charlie Gibbs system is formed by two narrow sub-parallel right-lateral transform faults (Johnson, 1967; Fleming et al., 1970). The ~ 110 km-long southern transform follows strictly the Wilson’s definition (Wilson, 1965) of an oceanic transform fault consisting of a single narrow

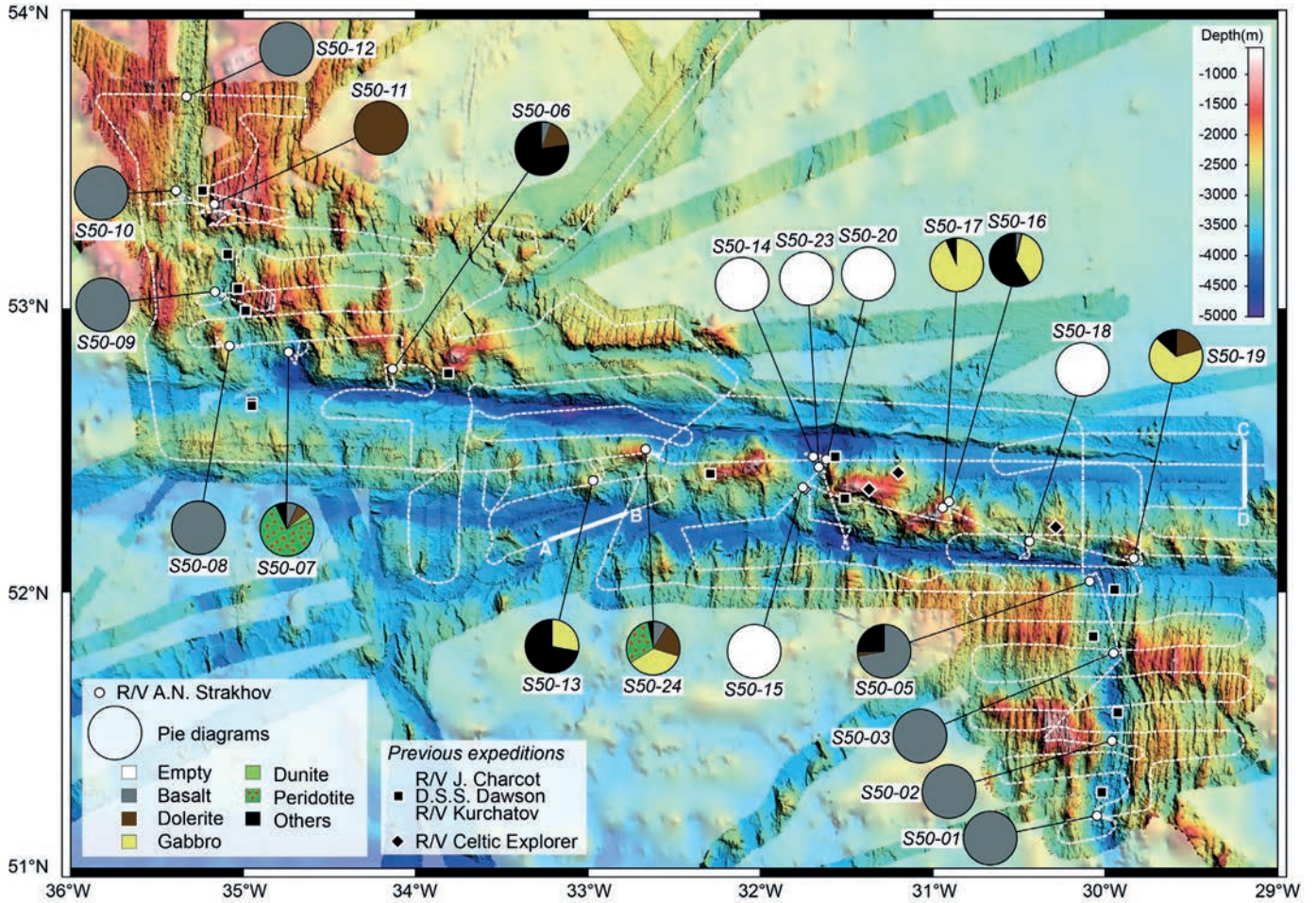


Fig. 2 - Compilation of bathymetric data including the high-resolution bathymetry acquired during cruise S50; previous data include the bathymetry from expeditions of the *R/V Jean Charcot* (Hekinian and Aumento, 1973), *R/V C.S.S. Dawson* (Hekinian and Aumento, 1973; Sigurdsson, 1981; Shilling et al., 1983), *R/V Kurchatov* (Chernysheva and Kharin, 2009) and the recent expeditions of the *R/V Celtic Explorer* (Georgiopoulou and CE18008 Scientific Party, 2018; Georgiopoulou et al., 2018; Marine Institute of Ireland, AORA Bathymetry database: [https://erddap.marine.ie/erddap/griddap/AORA\\_asc.html](https://erddap.marine.ie/erddap/griddap/AORA_asc.html), Furey, 2020). Location of dredge stations and the proportion of recovered lithologies are also reported as pie diagrams. Location of dredges deployed during previous expeditions are represented by black squares (Hekinian and Aumento, 1973; Blicher-Toft et al., 2005; Chernysheva and Kharin, 2009) and diamonds (cruise CE18008). The two white lines (A-B and C-D) mark locations of sub-bottom profiles shown in Fig. 7.

strike-slip zone that fits the small circle path with a root mean square error  $< 1$  km about the pole of rotation (Searle, 1981). In fact, a single very narrow lineament, trending  $95^\circ$  N, runs continuously along the active section marking the present day strike-slip principal displacement zone. The active part of the transform valley is almost free of sediments, although the sedimentary cover increases rapidly in the fracture zone valley to the east. The  $\sim 230$  km-long northern transform, in contrast to the southern one, displays greater seismicity with large magnitude earthquakes; it was affected by seven  $M \geq 6.25$  earthquakes over the past 100 years (Fig. 3, Aderhold and Abercrombie, 2016). This was the largest magnitude and longest repeat time sequences observed to date on an oceanic transform fault. The most significant episodes occurred in 1974 and 2015, with magnitudes of  $M_S$  6.9 and  $M_W$  7.1, respectively. Distribution of the seismic swarm events shows a western and an eastern sequence with a general migration of earthquake epicentres from the ridge towards the centre of the transform (Kanamori and Stewart, 1976; Bergman and Solomon, 1988). Aderhold and Abercrombie (2016) discussed how fault slip along transform segments accommodates seismically during large earthquakes and aseismically

in between. A thick sedimentary infill in the 20 km-wide active northern transform valley masks most of the basement structures (Searle, 1981).

Searle (1981) first showed the existence of a N-S trending,  $\sim 40$  km-long intra-transform spreading centre located at a longitude of  $\sim 31^\circ 45'$  W. The axial part of the ITR has been recently investigated by expeditions CE15007, CE16014 and CE18008 with the *R/V Celtic Explorer* that confirmed the occurrence of core complexes exhumed probably by low angle normal faults (Georgiopoulou and CE18008 Scientific Party, 2018; Georgiopoulou et al., 2018). Similar to what was documented in large transforms elsewhere (e.g., Prince and Forsyth, 1988; Bonatti et al., 2003), normal oceanic crust becomes thinner towards the transform, reaching a thickness of 3.5 km within the intra-transform domain (Whitmarsh and Calvert, 1986; Calvert and Whitmarsh, 1986).

Mapping in the '70s extends the Charlie Gibbs FZ to the east and west of the active offset region up to the Rockall Trough and the Labrador margin (e.g., Gaina et al., 2009; Keen et al., 2014; Peace et al., 2019). The continuity of the fracture zone from North America to Europe indicates that the transform was active since the early rifting stage

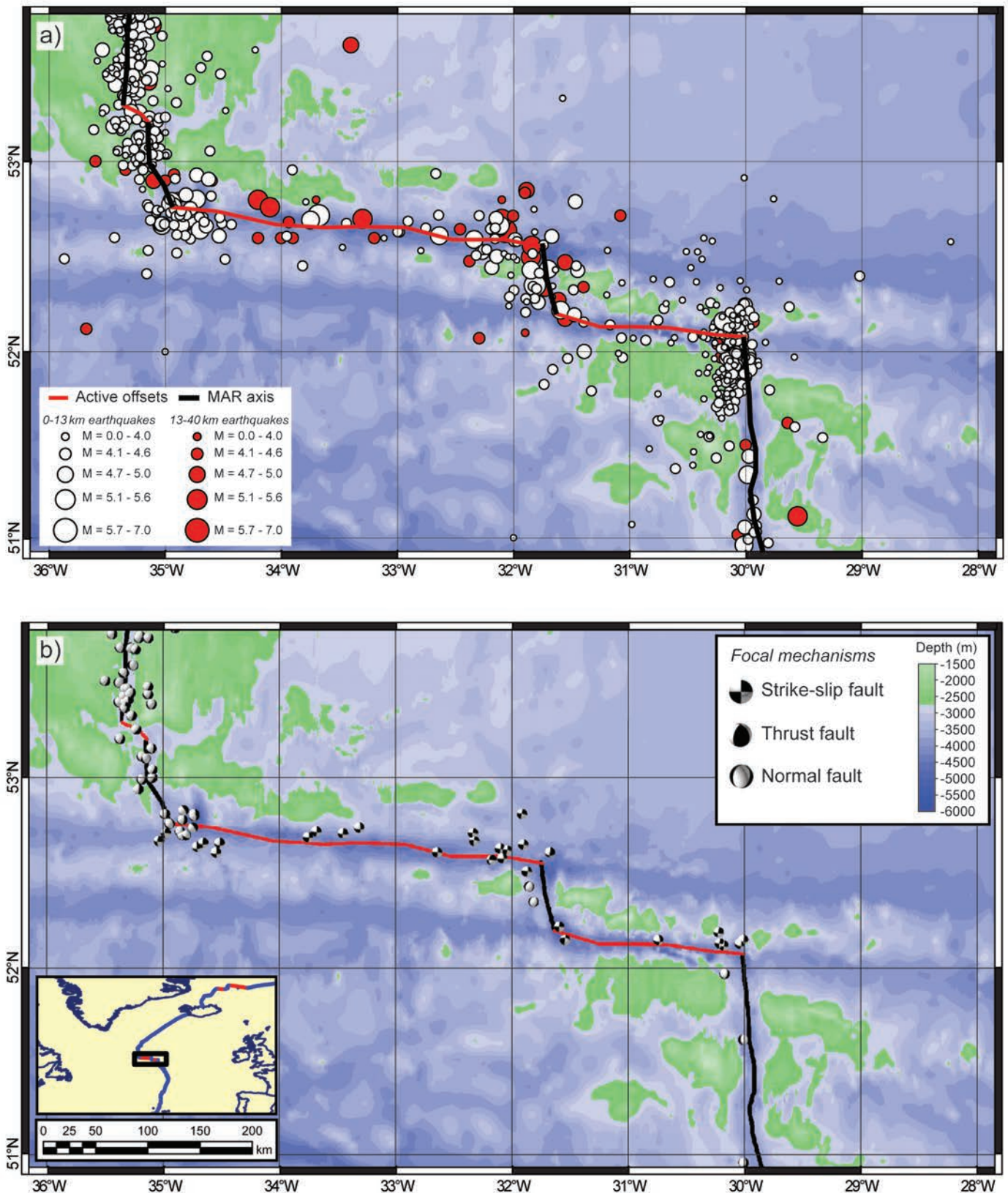


Fig. 3 - a) Seismicity of the Charlie Gibbs transform system from USGS earthquake catalog (<https://earthquake.usgs.gov/earthquakes/search>). b) Fault plane solutions from the Harvard global centroid moment tensor catalog (CMT, [www.globalcmt.org/CMTsearch.html](http://www.globalcmt.org/CMTsearch.html)).

between the Europe and North American plates (e.g., Olivet et al., 1970; 1974; Johnson et al., 1971; Roberts et al., 1979). Detailed studies on the Newfoundland oceanic lithosphere suggest contrasting structural styles of the margins north and south of the Charlie Gibbs FZ. This may reflect a north-south

change in lithospheric fabric across this fracture zone (Keen et al., 2014). The landward extension of the Charlie Gibbs FZ within the continental margin (Haworth, 1977) may intersect the Dover Fault, which marks the northwestern boundary of the Avalon Zone in Newfoundland. Consistently, Gaina and

Jakob (2018) recently suggested that changes in spreading rates and direction in the northern and southern portions of the Charlie Gibbs FZ might have occurred during the Eocene. These changes were possibly influenced by variations in the Pacific subduction rate or by plume activity in the Atlantic (Gaina and Jakob, 2018; Peace et al., 2019).

The Charlie Gibbs FZ is located at the southern edge of the Iceland plume regional topographic swell. It separates the Iceland and Azores domains of the Mid Atlantic Ridge. The difference in regional topography (Fig. 4a) correlates with a sharp change in basalt chemistry, with along axis variations in  $\text{Na}_8$  (Na contents normalized to  $\text{MgO} = 8 \text{ wt}\%$ ; Klein and Langmuir, 1987). The basalts from southern portions of the fracture zone have higher  $\text{Na}_8$  relative to those in the northern portion, indicating probably a progressive increase of average melting degrees at increasing latitude (Fig. 4b). Basaltic glasses from 51-54.0° N show compositions gradually more radiogenic in Pb (and Sr), and less radiogenic in Nd (and Hf) isotopes towards the intra-transform spreading centre (Schilling et al., 1993; Blichert-Toft et al., 2005).

Previous dredge expeditions were conducted in 1969 (Hekinian and Aumento, 1973), 1970 (Hekinian and Aumento, 1973; Sigurdsson, 1981) and in 1973 (*R/V Akademik Kurchatov*; Chernysheva and Kharin, 2009). Sample locations are mostly from the Minia Seamount near the northern intersection with the Reykjanes ridge, from the northern wall of the northernmost transform valley, along the ITR axial region and in the southern portion of the MAR (Fig. 2). Dredged material, collected from a depth range of 1,900-4,250 m, is dominated by basalts (plagioclase and pyroxene

tholeiites; see Hekinian and Aumento, 1973; Chernysheva and Kharin, 2009), with peridotites and gabbro exposed along the northern wall of the northern valley and at bathymetric highs related to the ITR domain. Locally, dredge hauls include also rocks of continental origin transported by icebergs.

## EXPEDITION AKADEMIK NIKOLAJ STRAKHOV 50

### Material and methods

During cruise S50 of the *R/V A. N. Strakhov* bathymetry, magnetics and sub-bottom profiles were acquired, and dredges were deployed. The research vessel is equipped with differential GPS and SEAPATH positioning system. Swath bathymetry is recorded by a 12 kHz RESON SEABAT-7150-P multibeam system, consisting of 234 beams ( $2 \times 2^\circ$ ) with a total aperture of  $150^\circ$ , capable to acquire data at full ocean depth. The raw data were processed using the RESON PDS-2000 software to produce bathymetric grids up to a grid cell resolution of 50 m. Real-time seawater velocity at transducers required for beamforming, was assured by a sound velocity probe hull-mounted 1 m above the Sonar Head and interfaced directly to the multibeam acquisition system. A total of 12 sound velocity profile casts were distributed homogeneously within the studied area and were integrated with the Levitus database for the deepest part of the water column. The total length of the acquired bathymetric profiles is 5,500 km, covering an area of  $\sim 55,000 \text{ km}^2$  (Fig. 2).

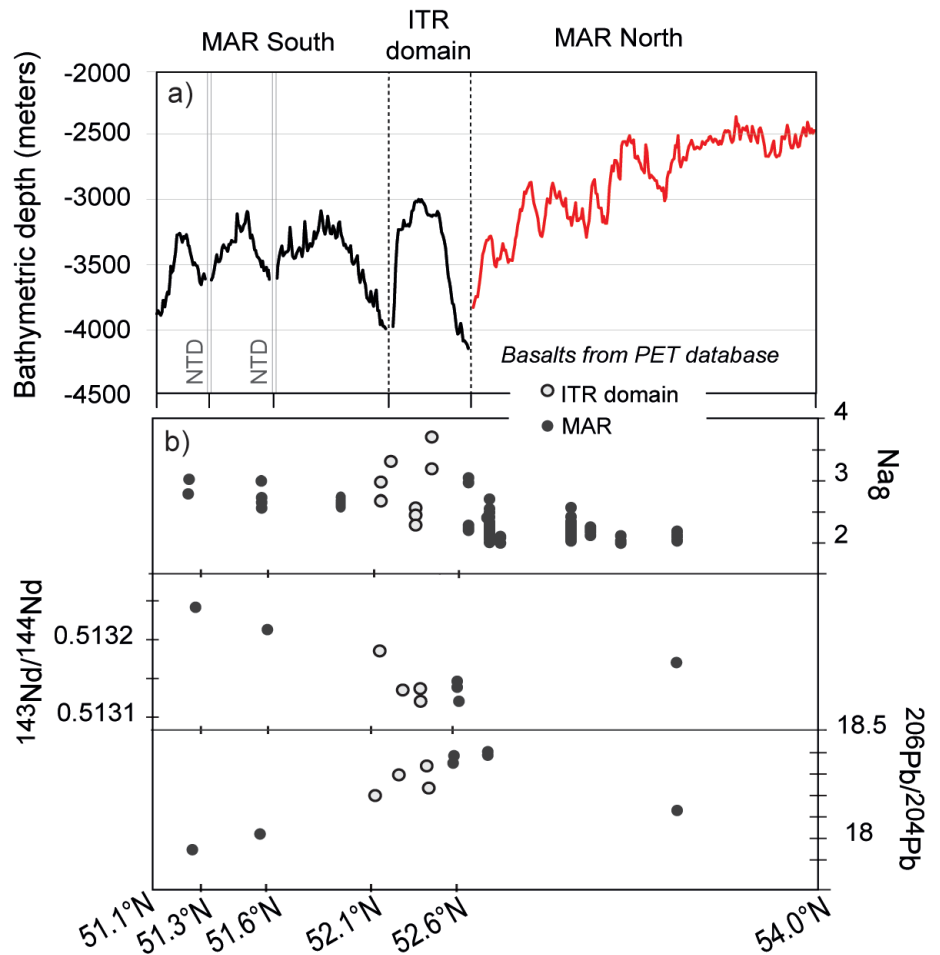


Fig. 4 - a) Axial depth profile along MAR South segment, intra-transform spreading centre and MAR North from S50 bathymetric grid; dotted vertical lines indicate the location of the transform valleys and the grey lines show the latitude of the two non-transform offsets (NTO) along MAR South. b) Along-axis compositional and isotopic variation of basalts in  $\text{Na}_8$ ,  $^{143}\text{Nd}/^{144}\text{Nd}$  and  $^{206}\text{Pb}/^{204}\text{Pb}$  downloaded from the PetDB Database ([www.earthchem.org/petdb](http://www.earthchem.org/petdb)) on 10 October, 2020. Samples within the Intra-Transform domain are represented by light grey dots and by black dots along MAR.

Single channel seismic reflection profiles were also acquired. The profiles were obtained using an EdgeTech 3,300 system (operating with 16 hull-mount transducers). The system, based on EdgeTech's Full Spectrum® Technology, generates a modulated long signal with frequency varying linearly from 2 to 6 kHz. The tapered waveform spectrum results in images that have virtually constant resolution with depth. Maximum sub-bottom penetration is 60-80 m with a vertical resolution of about 0.2-0.5 m.

Magnetic investigations were carried out with two marine magnetometers in a gradiometric configuration useful for reducing diurnal variations of the magnetic field. We deployed a Marine Magnetics SeaSpy (pulsed Overhauser magnetometer) and a Geometrics G882 (cesium magnetometer) system towed behind the vessel at a distance of 219 m and 253 m, respectively. The data were recorded at 1 Hz sampling rate using the Marine Magnetics SeaLink and the Geometrics MagLog softwares, respectively. The two systems have recorded similar and comparable total magnetic field values along the more than 3,800 km of acquired magnetic profiles. A preliminary data processing has been carried out on board using the SIO RAS software (Gorodnitskiy et al., 2013).

Seafloor sampling was carried out with cylindrical dredges for a total of 21 dredge stations of which 5 were empty. Most of the empty dredges were located in the intra-transform rift valley.

## MORPHOLOGY

The new bathymetric survey gave us the first complete high-resolution view of the Charlie Gibbs transform system (Fig. 2). The study area can be divided in 3 tectonic domains: i) the MAR South spreading segment, ii) the Charlie Gibbs transform domain, and iii) the MAR North spreading segment.

### MAR South

Seafloor formed by the MAR segment south of Charlie Gibbs (51.1 to 52.1° N) shows typical oceanic fabric (Fig. 5a). A non-transform offset (NTO), i.e., a second order discontinuity segmenting mid-ocean ridges with a spatial offset ranging from 15-30 km, where a gradual transition between adjacent spreading segments involves no significant transform faulting, (Spencer et al., 1997) at a latitude of 51.65°N shifts the northernmost MAR axial valley by ~ 7 km westward (Fig. 5a) reaching a maximum depth of 4,115 m. The axial displacement is subparallel to the Charlie Gibbs transforms and the discordant zones consist of a series of broad off-axis depressions interrupted by narrow oblique volcanic ridges. The MAR South axial valley runs on average along a direction of 8°N, orthogonal to the Charlie Gibbs transforms (Fig. 5a). The rift valley is narrow (10-12 km) and shows the highest relief (2,750-3,500 m) in its central sector due to short (10 km) and narrow (1.5 km) 100 m-high neovolcanic ridges (Figs 5b and c). The width and depth of the rift valley increase towards the NTO segment ends. Both sides of the axial valley show abyssal hills perpendicular to the spreading direction, consisting of an alternation of elongated ridges and narrow (up to 1 km) depressions. At 52.03°N and 31.47°W, a 25 km-long topographic high, culminating at a depth of 1800 m and furrowed by spreading-parallel corrugations, suggests the presence of an OCC formed probably as inner corner high at the MAR South and Charlie Gibbs southern transform intersection. It is now displaced westward of ~ 100 km relative to the ridge axis (Fig. 2).

### MAR North

The MAR North spreading segment shows a sharp discontinuity at 53.25°N (Fig. 6a). North from this discontinuity the ridge axis is straight and non-segmented with a direction of 8°N and has a rift valley with width and depth of ~ 15 km and 3,000 m, respectively. The rift valley is scattered by numerous neovolcanic ridges, showing sinuous shape and striking parallel to the main rift direction. Oceanic fabric typical of magmatic seafloor accretion characterizes both sides of the rift valley, forming hills lineated perpendicular to the spreading direction. Abyssal hills are higher (up to 1,500 m) and narrower (3-3.5 km) compared to the MAR South spreading segment (Fig. 6b). Locally, topographic highs (up to 915 m) interrupt the uniformity of this fabric, possibly representing isolate seamounts.

The regular structure of the MAR North spreading segment is interrupted southward at 53.25°N, where a non-transform discontinuity offsets the ridge axis by ~ 18 km. The inter-trough zone linking the two axial valleys at the NTO is 10 km wide with at its centre a large flat-top central volcano (diameter 3 km and height 250 m) and oblique lineaments dissecting the central depression (Fig. 6c).

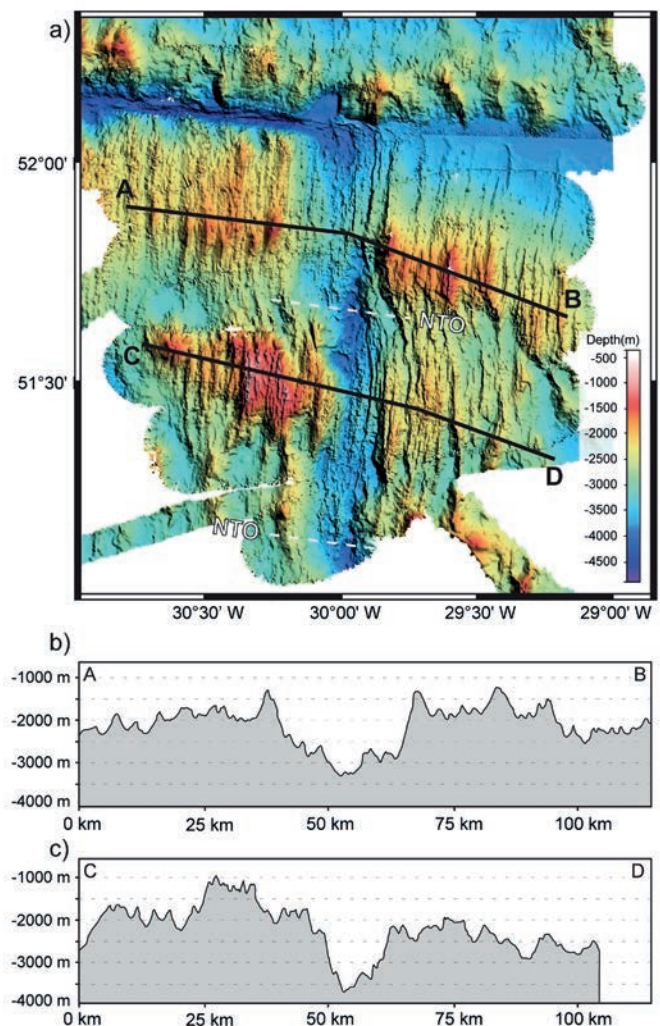


Fig. 5 - a) Bathymetric close-up of the MAR South spreading segment. Black lines indicate the location of the two depth profiles shown in b) and c). b) Profile A-B across the ridge axis north of the non-transform offset (NTO). c) Profile C-D across the ridge axis south of the NTO.

South of the 53.25°N NTO, a 30 km-long ridge segment shows an axial neovolcanic zone up to 200 m high. The width and depth of the axial valley increase from the central part of the ridge segment towards its southern end, where it reaches a width of 20 km and a depth of 3,000 m. Subparallel abyssal hills on both sides of the rift valley define an oceanic fabric similar to that observed at MAR South, although MAR North abyssal hills are shallower (Fig. 6).

Bathymetry and magnetic anomalies (see below), indicate a broader axial valley from 52.9°N to the Charlie Gibbs northern ridge-transform intersection (RTI). It reaches a width of 60-70 km and shows indistinct boundaries. The central sector of the rift valley is dominated by a large oblique (oriented NNW-SSE) neovolcanic ridge up to 700-800 m high, 4-5 km wide and 15-20 km long; its crest deepens into the transform valley. On the eastern side of this neovolcanic zone, a series of en-echelon rift basins transposes the axial valley eastward as it approaches the RTI. These basins with an average width of 4-5 km and depth of 3,400-3,500 m, are separated by small oblique (oriented NNW-SSE) neovolcanic ridges 100 m high, 1-2 km wide and 5-8 km long. A large

nodal basin (diameter 15 km and depth 4500 m) is located at the intersection with the transform valley representing probably the southernmost of these en echelon basins. Both sides of the axial zone show oblique fabric. Two large massifs 25 km long and 1,500 m high with clear corrugations (probably OCCs), are visible to the east of the ridge segment. These OCCs are bounded eastward by an E-W elongated depression at 52.8°N and 33.10°W; it may represent a paleo-transform valley because, north of it, the seafloor shows a well-defined N-S oceanic fabric.

### Charlie Gibbs

The Charlie Gibbs transform domain includes the northern and southern transform valleys, and the intra-transform region formed by lithosphere accreted at the ITR (Fig. 7).

#### *Intra-transform domain*

The present-day intra-transform spreading center, located at ~ 31.8°W, consists of a 40 km-long, 15 km-wide and deep (4,200 m) axial valley connecting the two transforms; it is shallower in its central part compared to the edges. Nodal basins with diameters of 20 and 30 km and depths 4,678 and 4,690 m are located at both intersections. A small volcanic ridge ~ 100 m high, 1.5 km wide and 2-7 km long occupies the northern part of the rift valley, while the southern part is characterized by a prominent ~ 800 m bathymetric high of uncertain nature, which penetrates into the south transform valley.

Large OCCs can be recognized on both shoulders of the rift valley: the western OCC is located at the inner corner of the intersection with the northern transform, whereas the eastern OCC is located at the outer corner (Fig. 7). Corrugated surfaces have an extension of ~ 30 and 68 km and maximum elevation of 1,100 m and 673 m for the western and eastern OCC, respectively. The seafloor within the intra-transform domain on both sides of the ITR exposes a series of smooth bathymetric highs with an average width of 25 km. The depth of these structures increases away from the rift valley (Fig. 7b) and some of them show corrugation on their tops. The crest of some of these bathymetric highs deepens into the transform valley, forming locally rounded shapes.

#### *Northern and southern transform valleys*

The northern and southern transform valleys have relatively different morphologies: both have the deepest (up to 4,500 m) and narrowest (up to 8 km) sectors in the active portion of the transform valleys, although the southern valley appears much narrower. The maximum depths are reached within the nodal basins and in an elongated basin at the center of the northern valley (33.17°W) reaching a depth of 4860 m. Conversely, the shallowest portions of the transform valleys are found in the areas adjacent the large OCCs.

The inactive sectors of the transform valleys are broader (up to 25 km) and shallower (up to 4,000 m) with flat seafloor and thick sediments (Fig. 7a). A ~ 35 km-long, ~ 6 km-wide and 250 m-high small median ridge is situated at the intersection between the northern transform and the intra-transform axial valley. This structure continues eastward into the passive part of the northern valley, where it reaches a length of ~ 160 km, a height of 800 m and width of 6 km. Small median ridges with length 30 km, width 5 km and height 200 m, are situated within the western part of the southern transform valley.

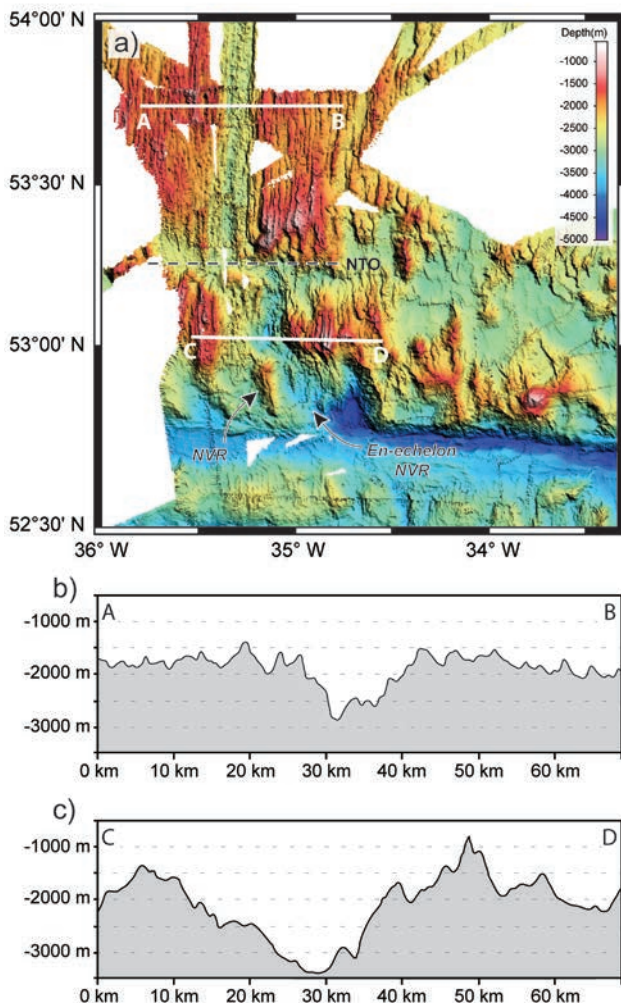


Fig. 6 - a) Bathymetric close-up of the MAR North spreading segment. White lines indicate the location of the two depth profiles presented in b) and c). b) Profile A-B across the ridge axis in the northernmost part of the ridge segment. c) Profile C-D across the ridge axis in the southernmost sector of the spreading segment. NVR, Neo-volcanic ridge.

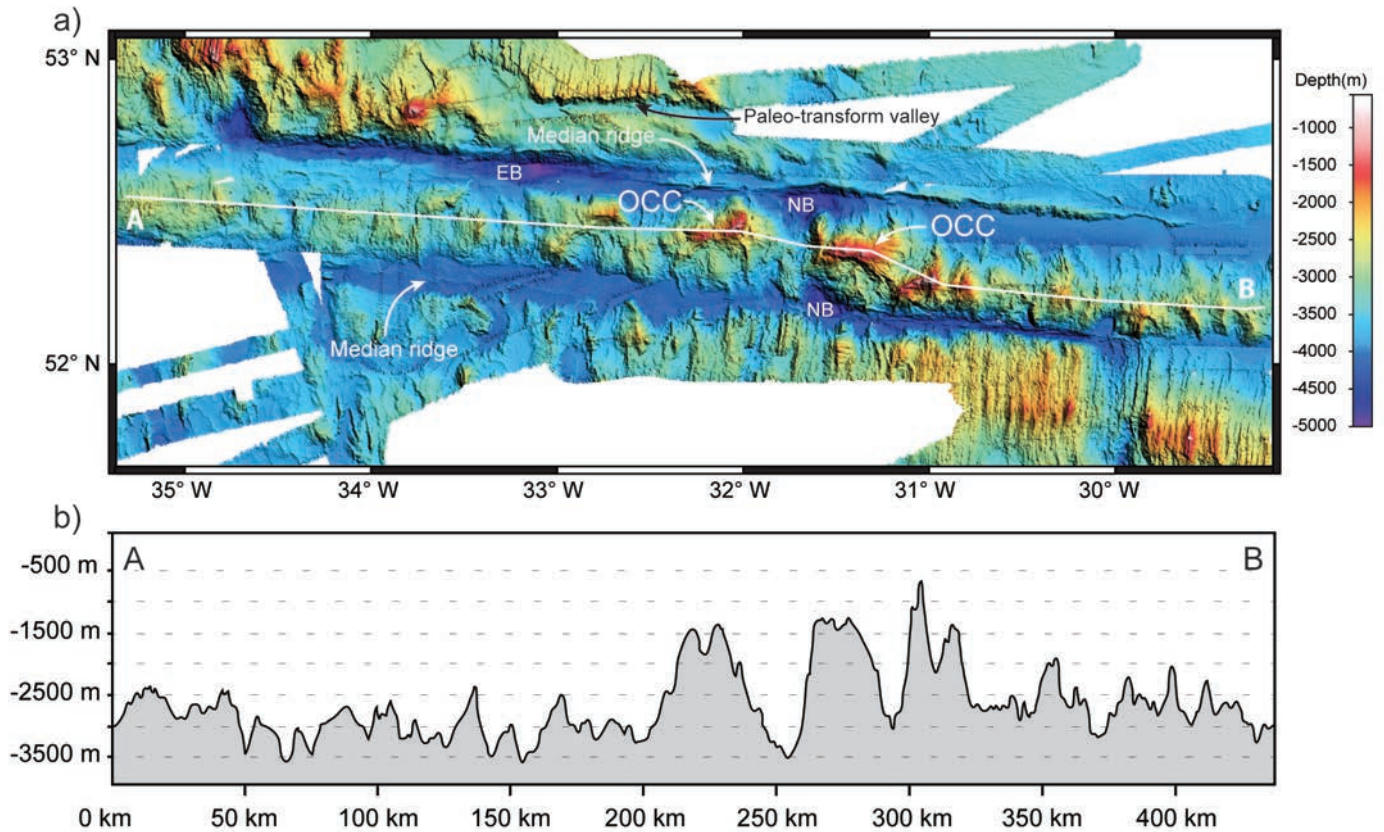


Fig. 7 - a) Bathymetric close-up of the intra-transform domain. White line indicates the location of the depth profile presented in b). b) Profile A-B running across the entire intra-transform domain from  $\sim 29^\circ$  W to  $\sim 35^\circ$  W and crossing the central part of the ITR axial valley. OCC, oceanic core complex; NB, nodal basin; EB, extinct nodal basin.

### SUB-BOTTOM PROFILES

The Charlie Gibbs region is characterized by high sedimentation rates up to 80 m/Ma (DSDP Leg 94, 1983) being located along the pathway of “Iceland-Scotland overflow water”. This dense water mass originates in the Nordic Seas and flows southwards in the deep Iceland Basin in multiple branches, one of which turns westwards through the Charlie-Gibbs FZ (Morozov et al., 2010).

The acquired sub-bottom profiles within the transform valleys resolve up to 60 m of unconsolidated stratified sediments interpreted as the uppermost portion (70-80 m) of a thick clastic sedimentary sequence above the magmatic basement. Seismic layers are mostly non-parallel to each other (except in the center of Fig. 8b), showing divergent geometries that often open towards the adjacent topographic high (Fig. 8a). The high resolution seismic profiles reveal a variety of sediment-drift and contourite deposits (Fig. 8a), according to their similarity with typical deposits reported in the literature (e.g., Marani et al., 1993; Rebesco and Stow, 2001). Chaotic deposits lacking of internal reflections are also observed and interpreted as mass transport deposits (MTD) from the valley walls.

Locally, in the inactive sector of the transform valleys, recent tectonic activity as normal faults and folds affects the sedimentary cover suggesting that within the transform domain shear deformation is not limited to the plate boundaries only (Fig. 8b). The tectonic nature of the box fold shown in Fig. 8b is revealed by on-lap geometries in the north side of

the fold and by the constant thickness of sedimentary seismic units on its top, in contrast with the sediment drift shown in Fig. 8a that shows thickness variability of the sedimentary sequences towards the crest of the structure.

### MAGNETIC SURVEY

The magnetic survey was carried out in the intra-transform domain and along the MAR South and North segments (Fig. 9). Magnetic data acquired during S50 cruise were complemented with those previously collected in the region (Searle, 1981; Merkuriev and DeMets, 2008) and extracted from the Marine & Geophysics NGDC database (<https://maps.ngdc.noaa.gov/viewers/geophysics>).

Almost 3,000 km of magnetics profiles are oriented east-west, hence roughly parallel to the spreading direction. In particular, the MAR South segment has been covered by equally spaced magnetic profiles (each  $\sim 100$  km long) crossing the two side of the ridge axis. In addition, a 200 km long magnetic survey, parallel and close to the southern transform fault, covers the western sector of the MAR South. Several magnetic profiles have been acquired across the eastern side of the MAR North segment, except for the northernmost profile which crosses the ridge axis parallel to the spreading directions for a total length of  $\sim 80$  km. Several short magnetic profiles were obtained within the intra-transform domain, while only one 400 km-long E-W profile crossing at its center the entire intra-transform domain has been acquired.

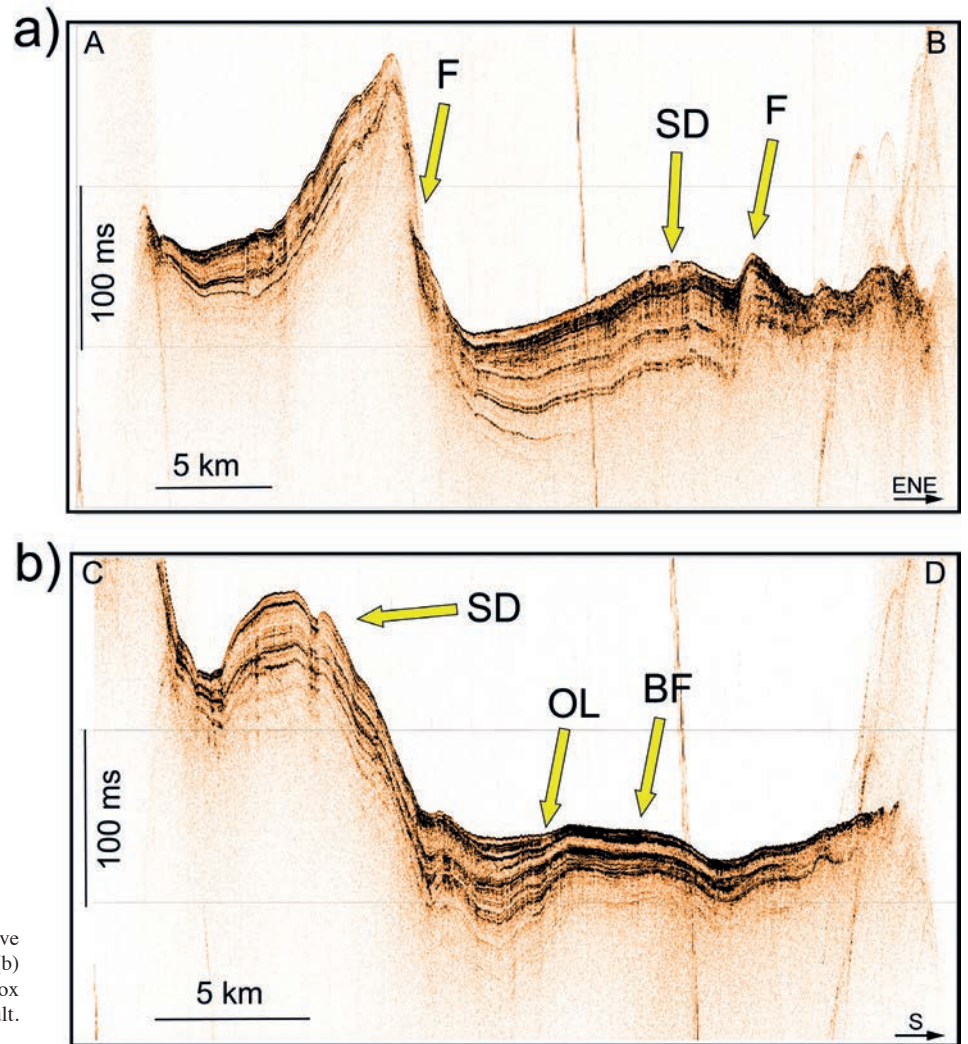


Fig. 8 - Sub-bottom profiles crossing the passive sectors of the southern (a) and the northern (b) transform valleys. SD- Sediment drift; BF- box fold; OL- onlap unconformity; F- normal fault. Locations of profiles are shown in Fig. 2.

Magnetic anomalies were obtained subtracting the International Geomagnetic Reference Field (IGRF-12, IAGA- Division V-MOD, [www.ngdc.noaa.gov/IAGA/vmod/igrf.html](http://www.ngdc.noaa.gov/IAGA/vmod/igrf.html)) from the observed total magnetic field. Preliminary results show different patterns within the survey area (Fig. 9). Profiles across the North and South MAR segments display a well-defined seafloor spreading pattern with a high-amplitude central anomaly flanked by alternating periods of reverse and normal magnetic polarity, while profiles crossing the intra-transform domain and along the two transform valleys show smooth and low magnetic anomalies with an anomalous wavelength. Magnetic anomalies correlated with synthetic profiles adopting the reference age model of Cande and Kent (1992) provide for the North and South MAR segments an average half spreading rate of  $\sim 10.8$  mm/a during the 0-2.5 Ma time interval (chron C1-C2A), a value comparable with literature data (Gaina and Jacob, 2018).

## LITHOLOGIES

During expedition S50,  $\sim 1,416$  kilograms of rocks were collected in 16 dredges deployed in different locations of the Charlie Gibbs Fracture Zone (Table 1 and Fig. 2), i.e., along the MAR South and MAR North segments, the north wall of the northern transform, and at three bathymetric highs in the

intra-transform domain. We describe next the recovered rock samples divided by lithology; only primary minerals were considered to estimate initial modal proportions, where possible we defined secondary minerals and alteration intensities. Mineral modal compositions were defined also macroscopically during the expedition. We followed the methods used during Expedition S45 (Skolotnev et al., 2020) to describe the extent of alteration, and crystal-plastic and brittle deformation intensities. To ensure consistency throughout the dredged hauls, each member of the Shipboard Party was responsible for one or more aspects of the description (e.g., rock type, textures, mineral modes, and habits). When possible, preliminary offshore microscopic analyses followed the shipboard observations in order to test the accuracy of the definition of rock types and deformation intensity. When present, iron-manganese coating was also reported. Vesicularity and phenocrysts were estimated in basalt samples, along with glass thickness. Crystal-plastic deformation intensity in peridotites was quantified based on foliation, grain size, and relative proportions of neoblasts.

Recovered samples include basalts (65 wt%), dolerites (6 wt%), gabbros (11 wt%), dunites (1 wt%), harzburgites (11 wt%) and drifted continental material (6 wt%) (Fig. 10a). They do not show mylonitic and ultramylonitic deformation. Instead, crystal plastic deformation (CPF) ranges from undeformed (grade 0) to foliated (grade 1) and weak

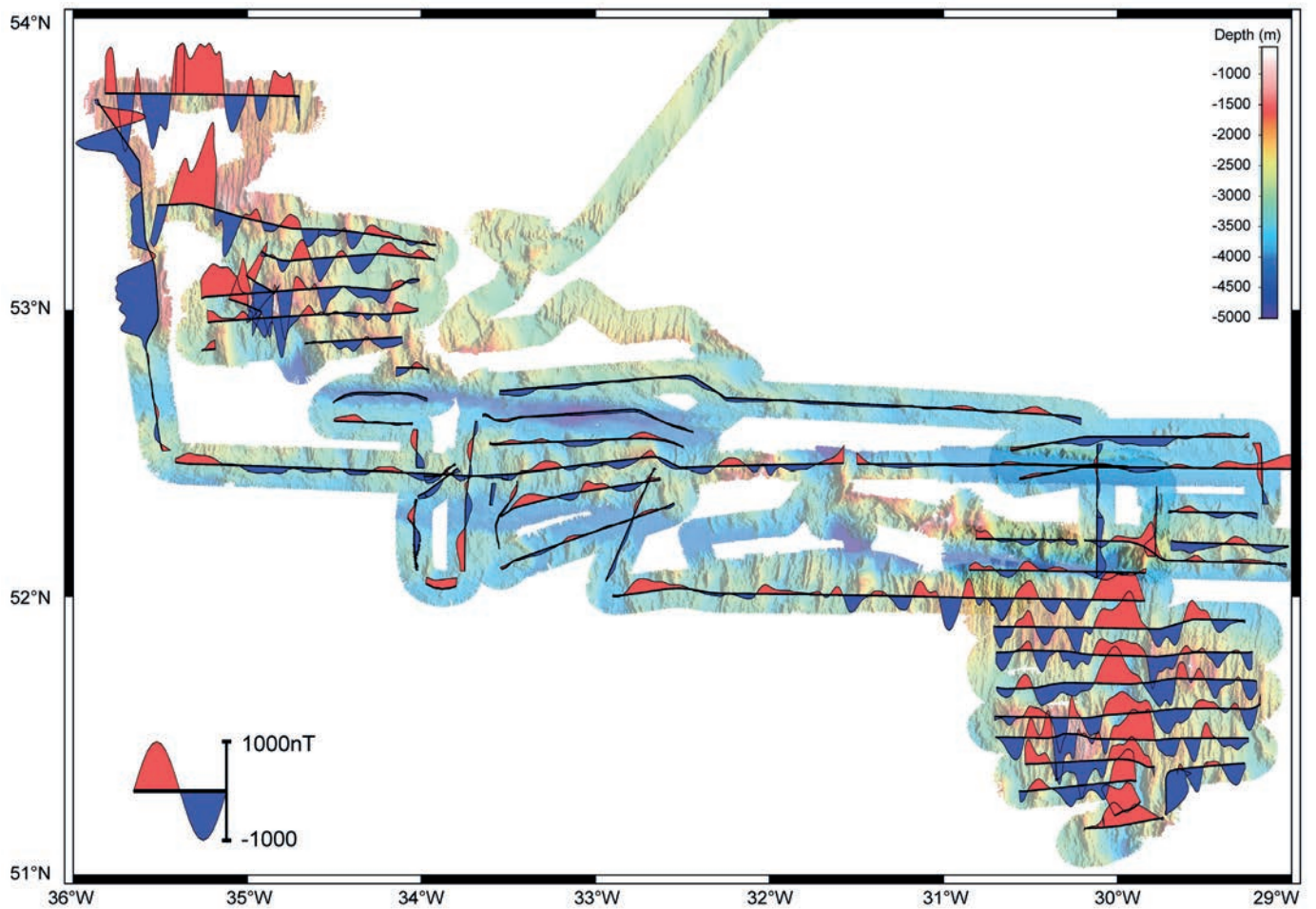


Fig. 9 - Magnetic anomalies of the Charlie Gibbs area superimposed to a shaded-relief image obtained using the swath bathymetry data. Red indicates positive magnetic anomalies, blue indicates negative anomalies.

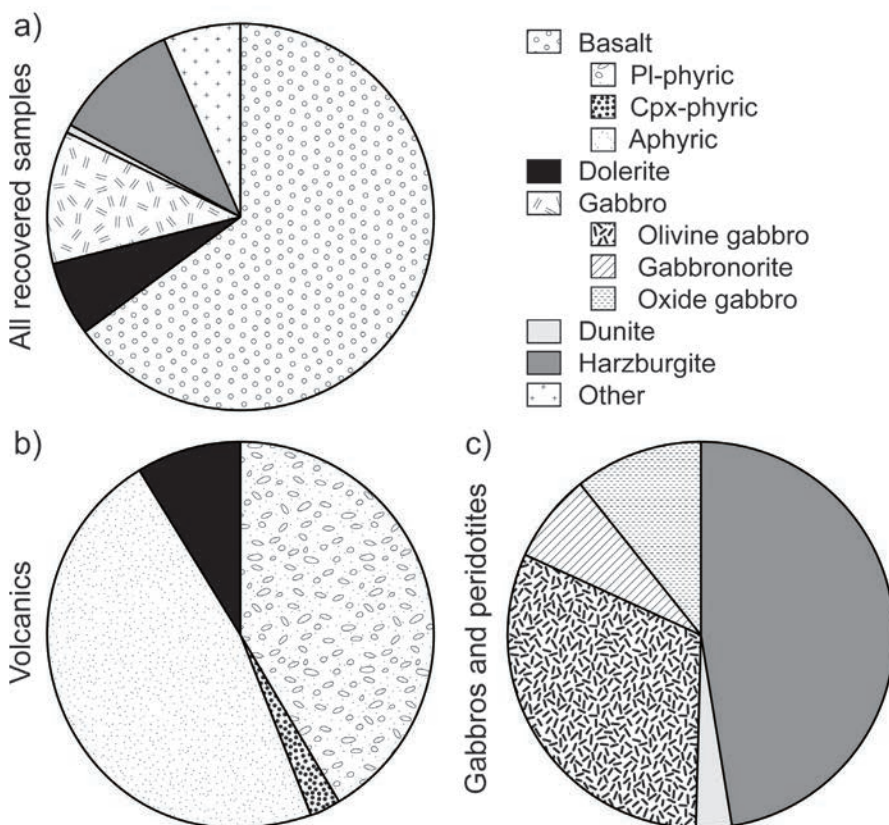


Fig. 10 - Modal proportion (pie diagrams) of the lithologies recovered during S50. a) Pie diagram of all recovered samples. b) Pie diagram of the volcanic rocks, including basalts and dolerites; c) Pie diagram of the mafic and ultramafic rocks, including olivine gabbros, gabbronorites, oxide gabbros, dunites and harzburgites.

Table 1 – Location and general description of dredges deployed during the S50 expedition.

Dredge	Location of dredging	On Bottom			Off Bottom			Contents (%)						Weight (kg)	
		Latitude [°N] (dd.ddd)	Longitude [°W] (dd.ddd)	Water depth (m)	Latitude [°N] (dd.ddd)	Longitude [°W] (dd.ddd)	Water depth (m)	Peridotite	Dunite	Gabbro	Dolerite	Basalt	Breccia		Others
S50-01	West shoulder of MAR SouthEast	51.188	-30.045	3610	51.192	-30.055	3600	-	-	-	-	100	-	-	329.1
S50-02	West shoulder of MAR SouthEast	51.450	-29.970	3690	51.453	-29.958	3610	-	-	-	-	100	-	-	67.57
S50-03	East flank of MAR SouthEast	51.777	-29.952	3830	51.780	-29.951	3790	-	-	-	-	100	-	-	380.71
S50-05	From nodal basin in intersection NW MAR SouthEast- FractureZone to West shoulder	52.051	-30.082	4090	52.043	-30.090	3720	-	-	-	2	70	-	28	35.2
S50-06	North wall of Fracture zone; 83.5 km from active MAR	52.767	-34.142	2300	52.795	-34.143	2100	-	-	-	-	21	-	79	26.5
S50-07	North wall of Fracture zone; 44 km from active MAR	52.835	-34.733	4000	52.848	-34.737	3800	78.5	4.5	-	-	7.5	-	9.5	206.5
S50-08	NorthWest; East flank of rift mountain	52.870	-35.060	3300	52.870	-35.073	3140	-	-	-	-	100	-	-	0.7
S50-09	From nodal basin to West shoulder of MAR NorthWest	53.060	-35.157	3300	53.057	-35.163	3200	-	-	-	-	100	-	-	71.15
S50-10	West shoulder of MAR NorthWest	53.401	-35.384	2510	53.413	-35.385	2470	-	-	-	-	100	-	-	1.3
S50-11	East flank of rift MAR NorthWest (N-S dredging)	53.362	v	1750	53.362	-35.167	1500	-	-	-	100	-	-	-	51.1
S50-12	West slope of seamount East of MAR NorthWest (another; N of Minia seamount)	53.685	-35.343	2880	53.735	-35.338	2850	-	-	-	-	99.5	-	0.5	16.9
S50-13	Slope shoulder of MAR NorthWest	52.397	-32.943	2850	52.402	-32.960	2550	-	-	-	-	-	29	71	0.6
S50-14	Slope West of 'caldera' West of ITR	52.478	-31.683	4370	52.477	-31.693	4130	-	-	-	-	-	-	-	-
S50-15	SW slope of nodal basin North of ITR SE flank of ITR; from nodal basin South of ITR to center of ITR	52.245	-31.667	4000	52.373	-31.748	3060	-	-	-	-	-	-	-	-
S50-16	East slope of high -bottom- (OCC?; deeper portion); 52.5 km to East of ITR	52.304	-30.922	2550	52.304	-30.927	2450	-	-	-	30.5	1	3	65.5	34.8
S50-17	East slope of high -top- (OCC?; shallower portion); 52.5 km to East of ITR	52.300	-30.942	2100	52.298	-30.953	1850	-	-	-	93.5	-	-	6.5	42.6
S50-18	West slope of high (OCC?); 87.65 km to East of ITR	52.142	-30.447	3500	52.180	-30.438	2600	-	-	-	-	-	-	-	-
S50-19	East slope of high (OCC?); 129.13 km to East of ITR	52.112	-29.838	3000	52.113	-29.842	2870	-	-	-	66.5	20	0.5	13	139.5
S50-20	West slope of high (OCC?); <5 km to East of ITR	52.472	-31.618	3650	52.472	-31.615	3350	-	-	-	-	-	-	-	-
S50-23	Base of west slope of high (OCC?); <5 km to East of ITR	52.438	-31.648	3950	52.443	-31.657	3900	-	-	-	-	-	-	-	-
S50-24	East slope of high (OCC?); 62 km to West of ITR	52.508	-32.660	2800	52.507	-32.675	2100	31	-	36	21	9	-	3	37.02

to strong porphyroclastic (grade 2 and 3, respectively). Brittle deformation (BT) ranges from undeformed (grade 0) to fractured (grade 1), brecciated without clast rotation (grade 2), densely fractured (grade 3), well-developed fault breccia (grade 4) and cataclastic with > 70% grain size reduction (grade 5). The occurrence and mineralogy of veins was also recorded.

### Basalts and dolerites

Basalts and dolerites were distinguished based on texture and/or the presence of volcanic glass, where dolerites have a crystalline matrix with subophitic texture and absence of glass. Basalts were recovered along the axes of MAR South (dredges S50-01, S50-02, S50-03) and MAR North segments (dredges S50-08, S50-09, S50-10, S50-12), in the nodal basins at the RTI between the MAR South and the southern transform (S50-05) and between the MAR North and the northern transform (S50-07). Basalts were sampled also along the northern wall of the northern transform (S50-06) and at three bathymetric highs within the intra-transform domain (S50-16, S50-19, east of the ITR and S50-24, west of the ITR; Fig. 2).

Fresh pillow basalts were recovered exclusively along the axes of the MAR South and MAR North segments. Nearly intact pillow basalts (Fig. 10a) show unaltered glass rims up to 20 mm in thickness (Fig. 11b). Smaller angular fragments show thinner unaltered to slightly palagonitized glass rims (< 8 mm). Few samples are decimetre-size tubular-shaped apophyses (Fig. 11c). Basalts from the other dredge hauls show low-temperature mineralizations containing smectites and Fe-hydroxides; these fragments are mainly rounded with thin Fe-Mn crust (< 1 mm). Overall, the vesicularity is lower than 5 vol%, with few samples showing up to 15 vol% vesicles.

The basalts range from aphyric (0 vol% phenocrysts) to sparsely phytic (< 5 vol% phenocrysts) and phytic (5–30 vol%) with typically a microcrystalline matrix. We classified the basalts in three groups based on the phenocryst contents and modes, namely: i) plagioclase-olivine basalts; ii) clinopyroxene basalts and iii) aphyric basalts.

#### Plagioclase-olivine basalts

represent 41% of the recovered volcanics. They were sampled mainly in dredges S50-01, S50-02, S50-03 in the southernmost sector of MAR South, and in dredge S50-12, in the northernmost sector of MAR North. Plagioclase is present as millimetre- to centimetre-size phenocrysts (Figs 11c and d) in variable modal contents, while minor olivine phenocrysts occur as millimetre-size crystals. Large intact pillow basalts are characterized by heterogeneous distribution of the phenocrysts that increase from crystal-poor pillow interior to the pillow rim (Fig. 11a) including the glass rim (Fig. 11c).

#### Clinopyroxene basalts

represent 2% of the recovered volcanics and have been sampled only in dredge S50-07. They contain millimetre-size phenocrysts of clinopyroxene (> 60 vol% of phenocrysts) and minor plagioclase (Fig. 11e). None of these samples have fresh glass rims.

#### Aphyric basalts

represent 48% of the recovered volcanics. They have been sampled in the northernmost sector of MAR South and southernmost sector of MAR North (S50-03, S50-05,

S50-08, S50-09, S50-10), and within the intra-transform domain. Their matrix ranges from microcrystalline to fine- and medium-grained.

#### Dolerites

represent 9% of the recovered rocks (Fig. 10b). They were sampled in the two nodal basins (S50-05, S50-07), on the northern wall of the North Transform (S50-06), at the off-axis seamount in the MAR North domain (S50-11) and on the three bathymetric highs within the Intra-Transform domain (S50-16, S50-19, S50-24). They are commonly characterized by a visible crystalline matrix presenting a subophitic texture (Fig. 11f). All dolerite samples are altered with substitution of the original clinopyroxene by chlorite and plagioclase by epidote and albite.

### Gabbros

Gabbros have been recovered exclusively within the intra-transform domain, at three bathymetric highs located at ~ 55 km and 130 km east (i.e., dredges S50-16 and S50-17, S50-19), and ~ 65 km west of the ITR (i.e., S50-24) (Fig. 2). We classified the gabbros in four groups based on the mineral modal compositions (Fig. 10c), namely olivine gabbros (63% of recovered gabbroic rocks), minor gabbro *sensu stricto* (<1%), gabbronorites (15%) and oxide gabbros (22%). All gabbros are undeformed and show isotropic magmatic fabrics.

#### Olivine gabbros (olivine > 5%) and Gabbro *s.s.*

are characterized by subophitic to ophitic textures of medium- to coarse-grained minerals (Fig. 12a and b). Grain-size variations are also observed at the scale of a single sample. Large poikilitic clinopyroxene oikocrysts, and less commonly olivine, contain elongated euhedral plagioclase chadacrysts. Plagioclase and clinopyroxene intergrowths occur in the ophitic olivine gabbros. Olivine gabbros from dredge S50-19 are modally primitive, (Ol ~ 25 vol%) and display pluricentimetre-size olivine crystals. Olivines are slightly serpentinized, showing the typical mesh textures, and variably weathered by clay minerals (Fig. 12a). One sample of olivine gabbro contains a felsic vein with sharp straight boundaries, composed probably of albitic plagioclase and amphibole; amphibole coronas developed around pre-existing pyroxenes along the contact with the host gabbro. Millimetre-size amphibole veins are observed locally crosscutting the Gabbros *s.s.* and Olivine gabbros.

#### Gabbronorites (orthopyroxene > 5%) and Oxide gabbros (Fe-Ti oxide > 5%)

are characterized by granular to subophitic textures of medium- to coarse-grained minerals (Fig. 12c and d). Both clinopyroxene and orthopyroxene show poikilitic textures and include elongated plagioclase laths. Fe-Ti oxides and amphiboles occur interstitially in Gabbronorites, whereas they commonly occur as discrete patches in Oxide gabbros. Orthopyroxene occurs sporadically in Oxide gabbros (Fig. 12d) and is often replaced by a fine-grained assemblage of clay minerals in both lithotypes (Figs. 12c and 12d).

### Peridotites

The recovered peridotites are harzburgites (olivine > 75 vol% and orthopyroxene > 15%) and minor dunites (> 90% olivine) (Fig. 10c). They were sampled in the nodal basin at

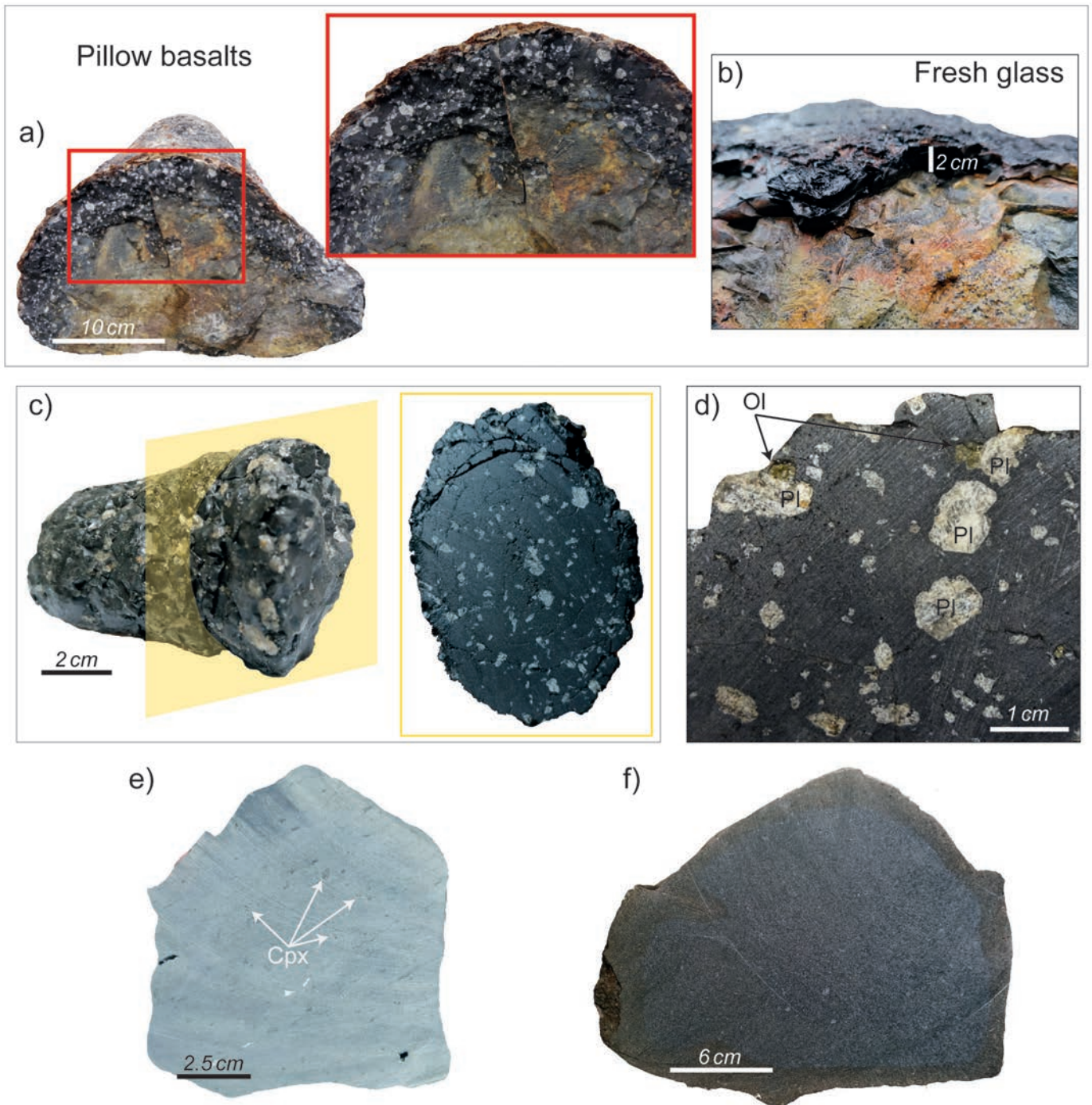


Fig. 11 - Hand-sample photographs of the volcanic rocks. a) Large Plagioclase-Olivine pillow basalt and close-up of the heterogeneous distribution of phenocrysts, from crystal-poor interior to crystal-rich pillow basalt rim. b) Thick glass rim of a large pillow basalt. c) Cylindrical phyrlic Plagioclase-Olivine basalt presenting a radial distribution of phenocrysts in the sectioned inset. d) Phyrlic Plagioclase-Olivine basalt characterized by centimetre-size plagioclase and millimetre-size olivine phenocrysts. e) Sparsely phyrlic Clinopyroxene-basalt containing elongated millimetre-size clinopyroxene phenocrysts. f) Medium-grained dolerite.

the RTI between the MAR North segment and the northern transform (S50-07), and on a bathymetric high west of the ITR (S50-24).

#### *Harzburgites*

(94 vol% of the recovered peridotites) display granular textures to weak porphyroclastic fabrics (CPF = 2; Fig. 13a and b) of medium- to coarse-grained minerals. They show variable mineral modal compositions, with local increase in

olivine contents towards dunitic compositions. These zones are commonly characterized by lobate contacts between olivine and pyroxenes, classically attributed to the overgrowth of olivine at the expense of pyroxenes. In these zones, spinels are abundant (~ 3-5 vol%) and often occur as irregular crystals forming trails. Few samples from the nodal basin (S50-07) show strong cataclastic deformation (BT = 5) with partly preserved harzburgite clasts embedded in a fine-grained matrix strongly altered by clay minerals (Fig. 13c).

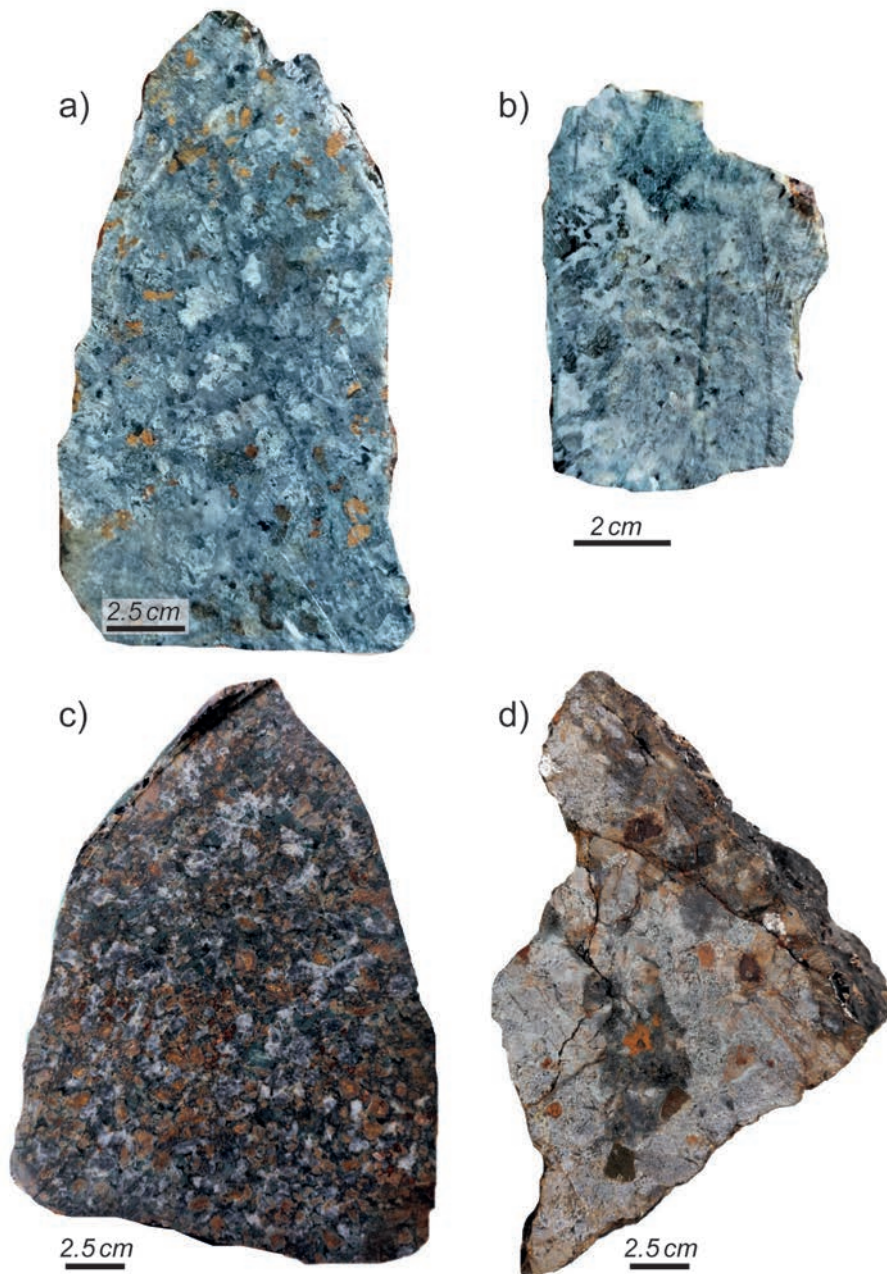


Fig. 12 - Hand-sample photographs of the gabbroic rocks. a) Coarse-grained olivine gabbro. b) Medium-grained gabbro. c) Coarse-grained gabbro-norite. d) Coarse-grained oxide gabbro

### Dunites

(6% of the recovered peridotites) are characterized by medium-grained spinel crystals and relicts of orthopyroxene displaying lobate contacts against olivine (Fig. 13d).

Veins are commonly observed in both harzburgites and dunites. Veins filled with serpentine are associated with widespread replacement of the rock-forming minerals by serpentine resulting from the interaction with seawater at temperature < 500°C (Fig. 13b). Additionally, olivines are typically replaced by clay minerals, classically attributed to superficial weathering. Less commonly, veins of aragonite crosscut the host peridotite (Fig. 13d).

### Exogenous and biogenic material

Drifted continental rocks have been recovered from the intra-transform domain (S50-13, S50-16, S50-17, S50-19, S50-24), in the two nodal basins (S50-05, S50-07) and along

the northern transform (S50-06) (Figs. 2 and 10a). They are made of rounded blocks of igneous and metamorphic rocks, including granites, tonalites, amphibolites and gneisses. Granites and tonalites show granular textures of medium- to coarse-grained minerals, and one granite sample includes a centimetre-size rounded lens of hornblende, partially corroded by the host granite (Fig. 14a). Amphibolites display weak foliations of plagioclase and amphibole and in one sample the foliation is folded (Fig. 14b). Gneisses are characterized by strong foliations of augen plagioclase crystals, quartz, and biotite, and occasionally by millimetre-size garnets (Fig. 14c).

Abundant fragments of fossil corals (*Desmophyllum dianthus*) were recovered from a depth of ~1,000 m at the S50-17 dredging site from the top of a bathymetric high within the intra-transform domain where gabbros were also sampled (Figs. 2 and 14d). Age determinations of these corals may constrain the timing of gabbro emplacement and lower crust

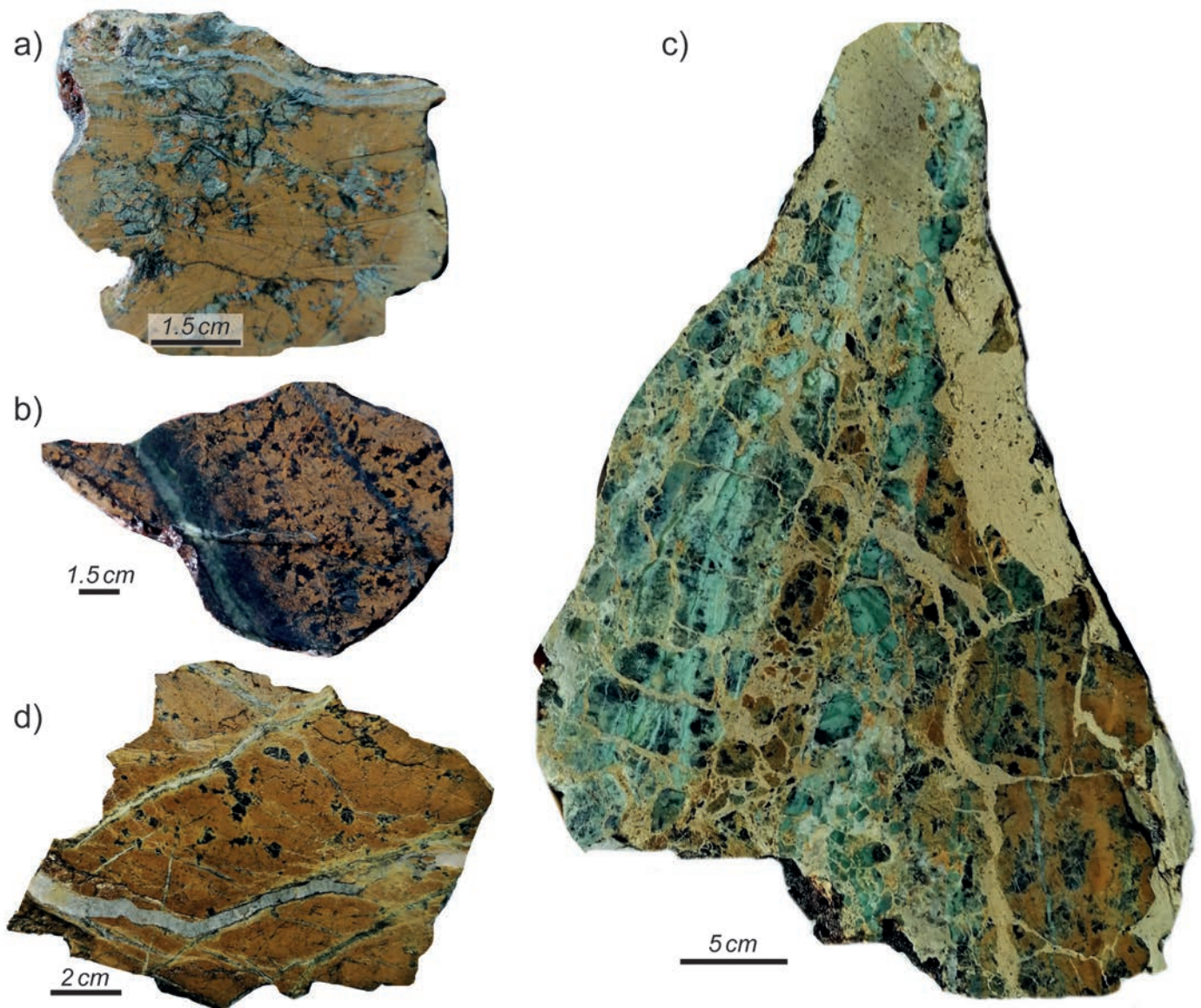


Fig. 13 - Hand-sample photographs of the ultramafic rocks. a) Coarse-grained harzburgite characterized by large pyroxene porphyroclasts. b) Medium-grained harzburgite characterized by altered pyroxene and spinel porphyroclasts. The sample includes millimetre- to centimetre-thick serpentine veins. c) Ultramafic cataclasite including preserved peridotite and serpentinite clasts. The sample shows a zonation of the intensity of deformation, from a relatively preserved part on the right side to stronger cataclastic deformation on the left side. d) Dunite with large spinel crystals and including a centimetre-thick aragonite vein.

exhumation. In addition, these deep-water scleractinian corals have an almost cosmopolitan geographic distribution and are excluded only from polar areas s.s. Their depth distribution ranges from the intertidal to 6,000 m, and they have a thermal tolerance between  $-1^{\circ}\text{C}$  to  $28^{\circ}\text{C}$ . Therefore, these corals potentially are excellent archives of past oceanographic conditions providing climate proxies for intermediate and deep waters (Taviani et al., 2005).

## DISCUSSION

Data from the S50 survey combined with swath bathymetry obtained during CE15, CE16014 and CE18008 (Georgiopoulou and CE18008 Scientific Party, 2018; Georgiopoulou et al. 2018; Furey, 2020), allow for the first time a complete large-scale view of the structure of Charlie Gibbs transform system better defining the morphological and structural set-

ting of the two parallel transform faults bounding the long-lived intra-transform domain. Present-day tectonic and magmatic activity is revealed by seismicity (Fig. 3). Earthquake data until 2019 were obtained from the US Geological Survey Earthquake Catalogue (USGS). Events with magnitude higher than 3 were plotted in Fig. 3a, after converting different magnitudes types to moment magnitude  $M_w$  (Lolli et al., 2014). Within the Charlie Gibbs transform domain, the seismicity is consistent with the morphological data, and shows earthquake epicenters clustered at the MAR North and MAR South spreading segments, and along the two transform faults (Fig. 3a). Focal mechanisms from the global Centroid Moment Tensor catalogue (Dziewonski et al., 1981; Ekström et al., 2012) show right-lateral strike-slip kinematics on near vertical E-W fault planes along the transform, and normal faulting perpendicular to seafloor spreading along the axial valleys of MAR North and South and within the rift valley of the intra-transform domain (Fig. 3b). Active spreading in

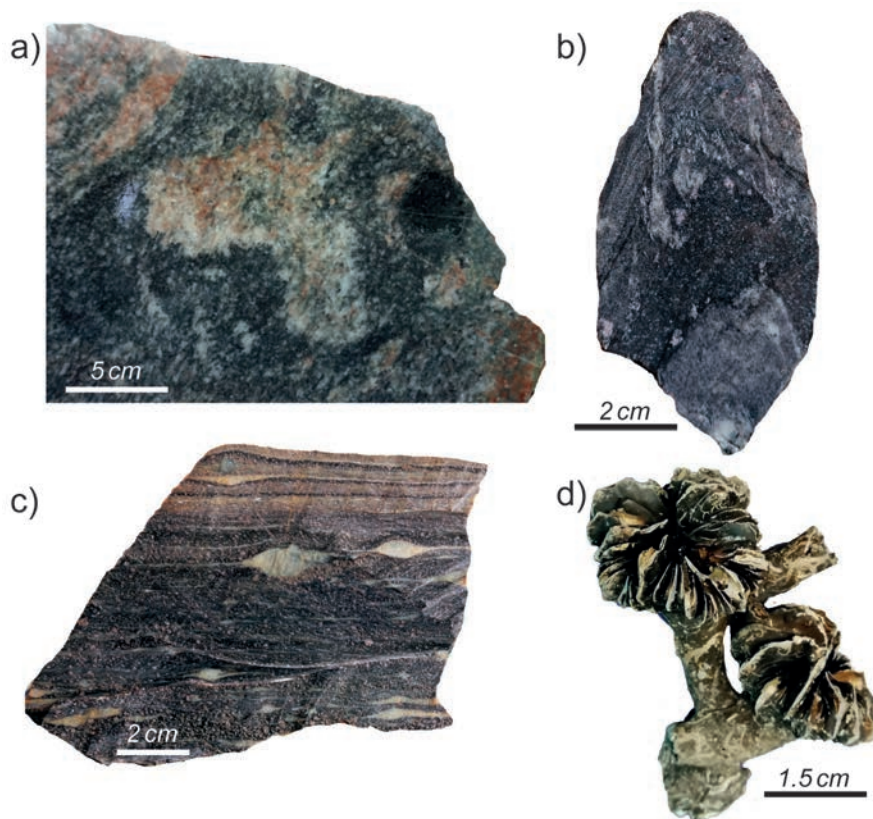


Fig. 14 - Hand-sample photographs of the continental rocks. a) Coarse-grained granite including an irregular centimetre-size hornblende lense. b) Folded amphibolite. c) Foliated garnet-bearing gneiss bearing centimetre-size augen plagioclase crystals. d) Corals from dredging site S50-17: *Desmophyllum dianthus*.

the intra-transform axial region is thereby confirmed by seismic clusters with normal fault plane solutions along the rift shoulders (Fig 3a and b). Interestingly, sub-bottom profiles at 33°W and 29.2°W (A-B and C-D in Fig.2) crossing the inactive portion of the northern and southern transform valleys, respectively, show recent deformation possibly affecting the uppermost part of the sedimentary cover, suggesting that tectonic activity is not restricted to the active segments of the two transform faults (Fig. 8). Despite an apparently regular large-scale structure, our data reveal an extreme variability of seafloor morphology that can be related ultimately to a strong variability in the tectonic conditions within this transform domain.

#### MAR South and North segments

MAR North and South segments are long spreading segments showing similar morphological characteristics away from the Charlie Gibbs region including few non-transform discontinuities. Despite this, the two segments reveal contrasting geomorphological variations approaching the fracture zone. The MAR South has a regular topography, with abyssal hills oriented perpendicular to the spreading direction and a typical volcanic seafloor up to the intersection with the southern transform (Fig. 5). Here, the axial valley intersects the transform fault without major changes in morphology such as the development of a deep nodal basin and/or an inner corner high. Fresh basalt glasses were sampled along axis and within the nodal basin (see Fig. 2). On the other hand, the morphology of the MAR North segment reveals a gradual transition from robust magmatism in the north to a highly-segmented magma-starved spreading segment approaching the transform fault in the south (Fig. 6).

Indeed, at 53.25°N the axial valley is shifted for ~ 18 km by a non-transform discontinuity defining a spreading segment with oblique structures and a broad valley up to the RTI. The magnetic survey supports this observation, showing normal magnetization centred along a neo-volcanic ridge oriented NNW-SSE (Fig. 9). The occurrence of lower crustal and mantle rocks on the flank of the nodal basin (S50-07, Fig. 2) suggests exhumation of basement rocks at the RTI. The architecture of the seafloor in this sector can be related to tectonic denudation, as proved by corrugated surfaces on a dome-like structure at ~ 34°W, interpreted as an OCC exhumed by detachment faulting.

#### Tectonic spreading within the Intra-Transform Domain

The 40 km-wide intra-transform domain is characterized by a series of large bathymetric highs. Their distribution is irregular, as they are centred either on the northern wall of the southern transform valley or on the southern wall of the northern transform valley (Fig. 2), almost bordering the active transform valley. These bathymetric highs become larger and shallower close to the shoulders of the ITR axis, while they deepen and decrease in size towards the edges of the domain (Fig. 7). Overall, they are dome-shaped structures; the shallowest display well-developed spreading-parallel corrugations. The dredge hauls deployed on top of three of these domes recovered mainly gabbros and peridotites, and locally dolerites (Fig. 2), suggesting exposure of lower oceanic rocks.

Morphology and lithology are in contrast with the regular volcanic fabrics observed in the MAR segments (Figs. 2, 5 and 6). Their dome-shaped structure, the corrugated surfaces and exposed lower crustal rocks are typical of OCCs

formed by long-lived detachment faulting (e.g., Escartin et al., 2008; MacLeod et al., 2009; Sanfilippo et al., 2018; Dick et al., 2019). The largest OCC, located on the eastern side of the RTI between the ITR and the northern transform, has been recently mapped in detail and sampled by ROV dives during expedition CE18008 with the *R/V Celtic Explorer* (Georgiopolou and Murton, 2018; Georgiopolou et al. 2018). They also reported corrugated surfaces and recovered lower oceanic crust and mantle material, interpreted as due to crustal exhumation along a low-angle detachment fault.

Data collected during expedition S50 together with those from previous cruises imply that the intra-transform domain is formed mostly by a series of OCCs, with no evidence of long-lived magmatic activity; a setting typical of poorly magmatic stretches of the MAR (e.g., Escartin et al., 2008; MacLeod et al., 2009; Smith et al., 2014) suggesting that the accretion is driven by tectonic spreading, accommodated mainly by faulting and lower crustal exhumation. Two principal dipping directions characterize the detachment surfaces of the OCCs; they dip either towards the east or towards the west. This and their widespread distribution suggest cyclic formation of OCCs during the continuous accretion of lithosphere within this domain.

## CONCLUSIONS AND OUTLOOK

This study provides the first complete and detailed view of the Charlie Gibbs transform system, consisting of two parallel right-lateral transform faults linked by a long-lived short intra-transform spreading centre. During expedition S50 of *R/V A.N. Strakhov*, we surveyed an area of 54,552 km<sup>2</sup> covering the entire transform system and the two adjacent MAR spreading segments. Seismicity and focal mechanisms are consistent with the regional architecture showing strike-slip motion along the transform faults and normal faulting along the MAR segments and within the ITR axial valley.

Despite an apparently regular large-scale structure, our survey reveals an extreme morphological variability of the seafloor amongst the different domains: the MAR North segment reveals a southward transition from robust magmatic linear accretion towards a highly-segmented spreading axis dominated by tectonic extension that led to the local exposure of basement rocks and rare formation of OCCs at the ridge-transform intersection. Tectonic extension also dominates lithospheric accretion at the ITR with a series of OCCs exposing gabbros and peridotites. Conversely, the MAR South segment shows a more regular topography, with a typical volcanic seafloor up to the intersection with the southern transform.

The variability in style of lithospheric accretion is mirrored by variations in regional topography and in geochemistry of erupted basalts. The northern MAR segment reveals a gradual deepening towards the transform, whereas the regional bathymetry is roughly constant from the ITR to the MAR South segment. Literature data on basalts suggest preliminarily a southward decrease in the mantle degree of melting, coupled probably with changes in thermal regime. New geochemical data on basalt glasses and associated basement rocks will shed light on the possible role of mantle heterogeneity on the formation of the Charlie Gibbs transform system, one of the most prominent tectonic features of the North Atlantic.

## ACKNOWLEDGMENTS

We thank Captain A. Nazarevskiy, and officers and crew of *R/V Akademik Nikolaj Strakhov*. We are indebted to A. Georgiopolou and B. Murton, and to the Marine Institute of Ireland for providing us with the Cruise Report and bathymetric data from the CE18008 expedition. This study was supported by the Russian Foundation for the Basic Research (RFBR, project no. 18-55-7806 Ital\_t, 18-05-00691, 18-05-00316), Russian Basic Research Program (projects no. 0135-2019-0050, 0135-2019-0076, 0136-2018-0025, 0149-2019-0006), by Accordo Bilaterale CNR/RFBR 2018-2020 (CUP-B36C17000250005) and by the Italian Programma di Rilevante Interesse Nazionale (PRIN\_2017KY5ZX8). We thank Anne Briaes and an anonymous reviewer for their constructive comments.

## REFERENCES

- Aderhold K. and Abercrombie R.E., 2016. The 2015 Mw 7.1 earthquake on the Charlie-Gibbs transform fault: Repeating earthquakes and multimodal slip on a slow oceanic transform. *Geophys. Res. Lett.*, 43: 6119-6128, doi: 10.1002/2016GL068802.
- Bergman E.A. and Solomon S.C., 1988. Transform fault earthquakes in the North Atlantic: Source mechanisms and depth of faulting. *J. Geophys. Res.*, 93: 9027-9057.
- Blichert-Toft J., Agranier A., Andres M., Kingsley R., Schilling J. G. and Albarède F., 2005. Geochemical segmentation of the Mid-Atlantic Ridge north of Iceland and ridge-hot spot interaction in the North Atlantic. *Geochim. Geophys. Geosyst.*, 6 (1), doi: 10.1029/2004GC000788.
- Bonatti E., 1978. Vertical tectonism in oceanic fracture zones. *Earth Planet. Sci. Lett.*, 37 (3): 369-379.
- Bonatti E., Peyve A., Kepezhinskas P., Kurentsova N., Seyler M., Skolotnev S. and Udintsev G. 1992. Upper mantle heterogeneity below the Mid-Atlantic Ridge, 0°-15° N. *J. Geophys. Res. Solid Earth*, 97: 4461-4476.
- Bonatti E., Ligi M., Gasperini L., Peyve A., Raznitsin Y. and Chen Y.J., 1994. Transform migration and vertical tectonics at the Romanche fracture zone, equatorial Atlantic. *J. Geophys. Res.*, 99: 21779-21802.
- Bonatti E., Ligi M., Brunelli D., Cipriani A., Fabretti P., Ferrante V., Gasperini L. and Ottolini L., 2003. Mantle thermal pulses below the Mid-Atlantic Ridge and temporal variations in the formation of oceanic lithosphere. *Nature*, 423, 499-505.
- Cande S.C. and Kent D.V., 1992. A new geomagnetic polarity time scale for the Late Cretaceous and Cenozoic, *J. Geophys. Res.*, 97 (B10): 13917-13951, doi: 10.1029/92JB01202.
- Calvert A.J. and Whitmarsh R.B., 1986. The structure of the Charlie-Gibbs Fracture Zone. *J. Geol. Soc. London*, 143: 819-821.
- Chernysheva E.A. and Kharin G.S., 2009. Magmatic rocks in the Charlie-Gibbs Fracture Zone, North Atlantic Ocean. *Petrology*, 17: 476-487.
- Dick H. J.B., MacLeod C.J., Blum P., Abe N., Blackman D.K., Bowles J.A., Cheadle M.J., Cho K., Ciazela J., Deans J.R., Edgcomb V.P., Ferrando C., France L., Ghosh B., Ildefonse B., John B., Kendrick M.A., Koepke J., Leong J.A.M., Liu C., Ma Q., Morishita T., Morris A., Natland J.H., Nozaka T., Pluemper O., Sanfilippo A., Sylvan J.B., Tivey M.A., Tribuzio R. and Viegas G., 2011. Dynamic accretion beneath a slow-spreading ridge segment: IODP Hole 1473A and the Atlantis Bank Oceanic Core Complex. *J. Geophys. Res. Solid Earth*, 116: 12631-12659, ISSN: 2169-9313, doi: 10.1029/2011JB016858.
- DSDP Leg 94, 1983. Site 611. Shipboard scientific party. DSDP, 1983 Init. Rep., 94: 471-590.
- Dziewonski A.M., Chou T.-A. and Woodhouse J.H., 1981. Determination of earthquake source parameters from waveform data for studies of global and regional seismicity. *J. Geophys. Res.*, 86: 2825-2852.

- Ekström G., Nettles M. and Dziewonski A.M., 2012. The global CMT project 2004-2010: Centroid-moment tensors for 13,017 earthquakes. *Phys. Earth Planet. Intern.*, 200-201: 1-9.
- Escartin J., Smith D.K., Cann J., Schouten H., Langmuir C.H. and Escrig S., 2008. Central role of detachment faults in accretion of slow-spreading oceanic lithosphere. *Nature*, 455: 790-794, doi: 10.1038/nature07333.
- Fleming H.S., Cherkis N.Z. and Heirtzler J.R., 1970. The Gibbs Fracture Zone: a double fracture zone at 52°30'N in the Atlantic Ocean. *Mar. Geophys. Res.*, 1: 37-45.
- Furney T., 2020. Atlantic Ocean Research Alliance (AORA) Bathymetry Data Marine Institute, Ireland.
- Gaina C. and Jakob J., 2018. Global Eocene tectonic unrest: Possible causes and effects around the North American plate. *Tectonophysics*, 760: 136-151. doi: 10.1016/j.tecto.2018.08.010.
- Gaina C., Gernigon L. and Ball P., 2009. Palaeocene-Recent plate boundaries in the NE Atlantic and the formation of the Jan Mayen microcontinent. *J. Geol. Soc. London*, 166 (4): 601-616, doi: 10.1144/0016-76492008-112.
- Georgiopolou A. and CE18008 Scientific Party (2018). R/V Celtic Explorer cruise CE18008, 13th May - 8th June 2018 (Galway - Galway): Tectonic Ocean Spreading and the Charlie-Gibbs Fracture Zone. Marine Institute, Galway, Ireland. Cruise Report, pp 24.
- Georgiopolou A., Murton B., Chaytor J., Collin P., Hollis S., Judge M., Krastel S., Nomikou P., Robert K., Yeo I., 2018. White paper for the exploration of the Charlie-Gibbs Fracture Zone, Central Atlantic. In Summary Report for the Atlantic Seafloor Partnership for Integrated Research and Exploration Science Planning Workshop, November 15-16, Silver Spring, MD: 53-54.
- Gorodnitskiy A.M., Brusilovskiy Yu.V., Ivanenko A.N., Filin A.M. and Shishkina N.A., 2013. New methods for processing and interpretation of marine magnetic anomalies and their application to structural research and oil and gas exploration in the Kuril forearc, the Barents Sea and the Caspian Sea, Russia. *J. Earth Sci. Front.*, 4: 73-85. <https://doi.org/10.1016/j.gsf.2012.06.002>.
- Haworth R.T., 1977. The continental crust northeast of Newfoundland and its ancestral relationship to the Charlie Fracture Zone. *Nature*, 266: 246-249.
- Hekinian R. and Aumento F., 1973. Rocks from the Gibbs Fracture Zone and Minia Seamount near 53°N in the Atlantic Ocean. *Mar. Geol.*, 14: 47-72.
- Johnson G.L., 1967. North Atlantic fracture zones near 53°N, *Earth Planet. Sci. Lett.*, 2: 445-448.
- Johnson G.L., Vogt P.R. and Schneider E.D., 1971. Morphology of the northeastern Atlantic and Labrador Sea. *Dt. Hydrogr. Z.*, 24: 49-73.
- Kanamori H. and Stewart G.S., 1976. Mode of the strain release along the Gibbs fracture zone, Mid-Atlantic ridge, *Phys. Earth Planet. Inter.*, 11: 312-332
- Keen C.E., Dafeo L.T. and Dickie K., 2014. A volcanic province near the western termination of the Charlie-Gibbs Fracture Zone at the rifted margin, offshore northeast Newfoundland. *Tectonics*, 33: 1133-1153, doi: 10.1002/2014TC003547.
- Klein E.M. and Langmuir C.H., 1987. Global correlations of ocean ridge basalt chemistry with axial depth and crustal thickness. *J. Geophys. Res.*, 92: 8089-8115.
- Ligi M., Bonatti E., Cipriani A. and Ottolini L., 2005. Water-rich basalts at mid-ocean ridge cold spots. *Nature*, 434: 66-69.
- Ligi M., Bonatti E., Gasperini L. and Poliakov A.N.B., 2002. Oceanic broad multifault transform plate boundaries. *Geology*, 30: 11-14.
- Lonsdale P. and Shor A., 1979. The oblique intersection of the Mid-Atlantic ridge with Charlie-Gibbs transform fault. *Tectonophysics*, 54: 195-209.
- MacLeod C.J., Searle R.C., Casey J.F., Mallows C., Unsworth M., Achenbach K. and Harris M., 2009. Life cycle of oceanic core complexes. *Earth Planet. Sci. Lett.*, 287: 333-344.
- Maia M., Sichel S., Briais A. et al., 2016. Extreme mantle uplift and exhumation along a transpressive transform fault. *Nature Geosci.*, 9: 619-624, ISSN: 1752-0894, doi: 10.1038/NGEO2759.
- Marani M., Argnani A., Roveri M. and Trincardi F., 1993. Sediment drifts and erosional surfaces in the central Mediterranean: seismic evidence of bottom current activity. *Sedim. Geol.*, 82: 207-220.
- Melson W.G., Hart S.R. and Thompson G., 1973. St. Paul's Rocks, Equatorial Atlantic: petrogenesis, radiometric ages and implications on sea-floor spreading. *Studies in Earth and Space Sciences, Geol. Soc. Amer. 132: A Memoir in Honor of Harry Hammond Hess*, doi.org/10.1130/MEM132: 241-
- Merkouriev S. and DeMets C., 2008. A high-resolution model for Eurasia-North America plate kinematics since 20 Ma. *Geophys. J. Int.*, 173 (3), 1064-1083.
- Morozov E.G., Demidov A.N., Tarakanov R.Y. and Zenk W., 2010. Abyssal channels in the Atlantic Ocean. Springer, Berlin Heidelberg, pp. 288, doi: 10.1007/978-90-481-9358-5.
- Olivet J.-L., Le Pichon X., Monti S. and Sichel R., 1974. Charlie-Gibbs fracture zone. *J. Geophys. Res.*, 79: 2059-2072.
- Olivet J.-L., Sichel B., Thonon P., Le Pichon X., Martinais J. and Pautot G., 1970. La faille transformante Gibbs entre le Rift et la marge du Labrador. *C.R. Acad. Sci., Paris*, 271: 949-952.
- Peace A.L., Welford J.K., Ball P.L. and Nirrengarten M., 2019. Deformable plate tectonic models of the southern North Atlantic. *J. Geodyn.*, 128: 11-37, doi: 10.1016/j.jog.2019.05.005.
- Prince R.A. and Forsyth D.W., 1988. Horizontal extent of anomalously thin crust near the Vema fracture zone from the three-dimensional analysis of gravity anomalies. *J. Geophys. Res. Solid Earth*, 93 (B7): 8051-8063.
- Rebesco M. and Stow D., 2001. Seismic expression of contourites and related deposits: a preface. *Mar. Geophys. Res.*, 22: 303-308.
- Roberts D.G., Montadert L. and Searle R.C., 1979. The western Rockall Plateau: stratigraphy and structural evolution. In: L. Montadert and D.G. Roberts (Eds.), Initial reports of the Deep Sea Drilling Project covering Leg 48 of the cruises of the Drilling Vessel Glomar Challenger, Brest, France to Aberdeen, Scotland, May-July, 1976, 48: 1061-1088, georefid:1981-006448.
- Sanfilippo A., Dick H.J.B., Marschall H., Lissenmeberg J. and Urann B., 2018. Emplacement and high-temperature evolution of gabbros of the 16.5°N oceanic core complexes (Mid-Atlantic Ridge): insights into the compositional variability of the lower oceanic crust. *Geochem. Geophys. Geosyst.*, 20(1): 46-66, doi.org/10.1029/2018GC007512.
- Schilling J.-G., Zajac M., Evans R., Johnston T., White W., Devine J.D. and Kingsley R., 1983. Petrologic and geochemical variations along the Mid-Atlantic Ridge from 29°N to 73°N. *Am. J. Sci.*, 283: 510-586.
- Searle R., 1981. The active part of Charlie-Gibbs fracture zone: a study using sonar and other geophysical techniques. *J. Geophys. Res.*, 86: 243-262.
- Sigurdsson H., 1981. First-order major element variation in basalt glasses from the Mid-Atlantic Ridge: 29°N to 73°N. *J. Geophys. Res.*, 86: 9483-9502.
- Skolotnev S.G., Sanfilippo A., Peyve A.A., Muccini F., Sokolov S.Y., Sani C., Dobroliubova K.O., Ferrando C., Chamov N.P., Palmiotto C., Pertsev A.N., Bonatti E., Cuffaro M., Gryaznova A.C., Sholukhov K.N., Bich A.S. and Ligi M., 2020. Large-scale structure of the Doldrums multi-fault transform system (7-8°N Equatorial Atlantic): preliminary results from the 45<sup>th</sup> expedition of the R/V A.N. Strakhov. *Ofioliti*, 45: 25-41.
- Smith D., Schouten H., Dick H.J.B., Cann J., Salters V., Marschall H., Sanfilippo A., Ji F., Zhelezov A., Parnell-Turner R., Bai H., Junkin W., Urann B., Curry S., Sulanowska M. and Dick S., 2014. Development and evolution of detachment faulting along 50 km of the Mid-Atlantic Ridge near 16.5N. *Geochem. Geophys. Geosyst.*, 15 4692-4711, doi: 10.1002/2014GC005563.
- Smoot N.C. and Sharman G.F., 1985. Charlie-Gibbs: A fracture zone ridge. *Tectonophysics*, 116: 137-142.
- Spencer S., Smith D.K., Cann J.R., Lin J. and McAllister E., 1997. Structure and stability of non-transform discontinuities on the Mid Atlantic Ridge between 24°N and 30°N. *Mar. Geophys. Res.*, 19: 339-362.

- Srivastava S.P. and Verhoef J., 1992. Evolution of Mesozoic sedimentary basins around the North Central Atlantic: A preliminary plate kinematic solution. In: J. Parnell (Ed.), Basins on the Atlantic Seaboard: Petroleum geology, sedimentology and basin evolution. Geol. Soc. London Spec. Publ., 62: 397-420.
- Srivastava S.P., Verhoef J. and Macnab R., 1988a. Results from a detailed aeromagnetic survey across the northeast Newfoundland margin. Part I: Spreading anomalies and relationship between magnetic anomalies and the ocean-continent boundary. Mar. Pet. Geol., 5: 306-323.
- Srivastava S.P., Verhoef J. and Macnab R., 1988b. Results from a detailed aeromagnetic survey across the northeast Newfoundland margin. Part II: Early opening of the North Atlantic between the British Isles and Newfoundland. Mar. Pet. Geol., 5: 324-337.
- Taviani M., Freiwald A. and Zibrowius H., 2005. Deep coral growth in the Mediterranean Sea: an overview. In: A. Freiwald and J.M. Roberts (Eds), Deep-water corals and ecosystems. Springer, Berlin Heidelberg, p. 137-156.
- Vogt P.R. and Avery O.E., 1974. Detailed magnetic surveys in the Northeast Atlantic and Labrador Sea. J. Geophys. Res., 79: 363-389.
- Whitmarsh R.B. and Calvert A.J., 1986. Crustal structure of Atlantic fracture zones - I. The Charlie-Gibbs Fracture Zone. Geophys. J. R. Astr. Soc., 85: 107-138.
- Wilson J.T., 1965. A new class of faults and their bearing on continental drift. Nature, 207: 343-347.

Received, November 22, 2020

Accepted, January 15, 2021

